Timms, N. E. et al. (2019) New shock microstructures in titanite (CaTiSiO5) from the peak ring of the Chicxulub impact structure, Mexico. *Contributions to Mineralogy and Petrology*, 174(5), 38. (doi: [10.1007/s00410-019-1565-7](http://eprints.gla.ac.uk/192763/))

The material cannot be used for any other purpose without further permission of the publisher and is for private use only.

There may be differences between this version and the published version. You are advised to consult the publisher's version if you wish to cite from it.

[http://eprints.gla.ac.uk/192763/](http://eprints.gla.ac.uk/192763/)

Deposited on 29 May 2019

1    **New shock microstructures in titanite (CaTiSiO$_5$) from the peak ring**

2    **of the Chicxulub impact structure, Mexico**

3    Nicholas E. Timms[1], Mark A. Pearce[2], Timmons M. Erickson[1,3], Aaron J. Cavosie[1],

4    Auriol S.P. Rae[4,5], John Wheeler[6], Axel Wittmann[7], Ludovic Ferrière[8], Michael H.

5    Poelchau[5], Naotaka Tomioka[9], Gareth S. Collins[4], Sean P. S. Gulick[10], Cornelia

6    Rasmussen[10], Joanna V. Morgan[4] and the IODP-ICDP Expedition 364 Scientists*

7    *[1] The Institute for Geoscience Research (TIGeR), Space Science and Technology*

8    *Centre, School of Earth and Planetary Sciences, Curtin University, Perth, GPO Box*

9    *U1987, WA 6845, Australia*

10   *[2] CSIRO Mineral Resources, Australian Resources Research Centre, 26 Dick Perry*

11   *Avenue, Kensington, WA 6151, Australia*

12   *[3] Jacobs – JETS, NASA Johnson Space Center, Astromaterials Research and*

13   *Exploration Science Division, Mailcode XI3, 2101 NASA Parkway, Houston, TX, USA*

14   *[4] Department of Earth Science and Engineering, Imperial College London, London,*

15   *UK*

16   *[5] Institut für Geo- und Umweltnaturwissenschaften, Albert-Ludwigs-Universität,*

17   *Freiburg, Albertstraße 23b, 79104 Freiburg, Germany*

18   *[6] Department of Earth and Ocean Sciences, University of Liverpool, Liverpool, L69*

19   *3GP, UK*

20   *[7] Eyring Materials Center, Arizona State University, Tempe, AZ, USA*

21   *[8] Natural History Museum, Vienna, Austria*

22   *[9] Kochi Institute for Core Sample Research, Japan Agency for Marine-Earth Science*

23   *and Technology, Kochi, Japan.*

24   *[10] Institute for Geophysics and Department of Geological Sciences, Jackson School of*

25   *Geosciences, University of Texas at Austin, Austin, TX, USA*

26    *See full list and affiliations at the end of the manuscript text file.

27

28

29    **ABSTRACT**

30    Accessory mineral geochronometers such as apatite, baddeleyite, monazite, xenotime

31    and zircon are increasingly being recognized for their ability to preserve diagnostic

32    microstructural evidence of hypervelocity-impact processes. To date, little is known

33    about the response of titanite to shock metamorphism, even though it is a widespread

34    accessory phase and a U-Pb geochronometer. Here we report two new mechanical

35    twin modes in titanite within shocked granitoid from the Chicxulub impact structure,

36    Mexico. Titanite grains in the newly acquired core from the International Ocean

37    Discovery Program Hole M0077A preserve multiple sets of polysynthetic twins, most

38    commonly with composition planes $(K_1) = \sim\{\bar{1}11\}$, and shear direction $(\eta_1) = <110>$,

39    and less commonly with the mode $K_1 = \{130\}$, $\eta_1 = \sim<522>$. In some grains, $\{130\}$

40    deformation bands have formed concurrently with the deformation twins, indicating

41    dislocation slip with Burgers vector $\mathbf{b} = <341>$ can be active during impact

42    metamorphism. Titanite twins in the modes described here have not been reported

43    from endogenically-deformed rocks; we therefore propose that these newly identified

44    twin form as a result of shock deformation. Formation conditions of the twins has not

45    been experimentally calibrated, and is here empirically constrained by the presence of

46    planar deformation features in quartz ($12 \pm 5$ and $\sim17 \pm 5$ GPa) and the absence of

47    shock twins in zircon (<20 GPa). While the lower threshold of titanite twin formation

48    remains poorly-constrained, identification of these twins highlight the utility of

49    titanite as a shock indicator over the pressure range between 12-17 GPa. Given the

50    challenges to find diagnostic indicators of shock metamorphism to identify both

51 ancient and recent impact evidence on Earth, microstructural analysis of titanite is

52 here demonstrated to provide a new tool for recognizing impact deformation in rocks

53 where other impact evidence may be erased, altered, or did not manifest due to

54 generally low (<20 GPa) shock pressure.

55

58
59 **INTRODUCTION**

60 Identifying and dating impacts is essential to understand their role in key processes in

61 Earth history, such as mass extinctions (e.g. Hildebrand et al. 1991) and even the

62 proposed relation to the onset of plate tectonics (O'Neill et al. 2017). Recent

63 crystallographic and microstructural studies of datable accessory minerals like zircon

64 (e.g. Moser et al. 2011; Timms et al. 2012; Erickson et al. 2013; Cavosie et al. 2016a;

65 Cavosie et al. 2018a; Crow et al. 2018), monazite (e.g. Erickson et al. 2016; Erickson

66 et al. 2017a), baddeleyite (e.g. Darling et al. 2016; Timms et al. 2017a; White et al.

67 2018), and xenotime (Cavosie et al. 2016b) have greatly expanded the potential to

68 both recognize and date impact events (e.g. Erickson et al. 2017b). Titanite

69 ($CaTiSiO_5$) is a widely-utilized U-Pb geo- and thermochronometer that occurs in a

70 broad range of potential target rock compositions (Frost et al. 2001), including

71 metamorphic, sedimentary, and felsic to mafic igneous rocks. We report a detailed

72 electron backscatter diffraction (EBSD) microstructural study of impact deformation

73 in titanite, focusing on samples of shocked granitoid from the 2016 International

74 Ocean Discovery Program (IODP)-International Continental scientific Drilling

75 Program (ICDP) Expedition 364, that drilled the peak ring of the 200 km wide

76 Chicxulub impact structure off the coast of the Yucatán Peninsula (Morgan et al.

3

77    2017). We further demonstrate how these features can be distinguished from

78    deformation of titanite due to endogenic tectonic stresses.

79

80    **Titanite crystallography, microstructure, and deformation**

81         Titanite, formerly known as sphene until renamed by the International

82    Mineralogical Association (Hey 1982), has the nominal formula $CaTiSiO_5$, with an

83    atomic structure comprising chains of octahedral 6-fold Ti and 4-fold Si, with Ca

84    occupying a seven-fold site (Higgins and Ribbe 1976; Speer and Gibbs 1976). At

85    ambient pressure and temperature, titanite is monoclinic, and belongs to the space

86    group family $P2_1/a$ (Speer and Gibbs 1976; Taylor and Brown 1976). Above 496 °K

87    (223 °C), displacements of adjacent octahedral Ti chains define a transition to an

88    intermediate structure (Kunz et al. 1996). Above 825 °K (552 °C), or above ~3.5 GPa

89    at room temperature, further modification of the structure results in an orthorhombic

90    A2/a symmetry that accommodates a volume reduction of 5.1% (Salje et al. 1993;

91    Kunz et al. 1996; Angel et al. 1999). Titanite melts at >1380 °C (Hayward and

92    Cecchetto 1982).

93         Titanite has good cleavage along {110}, and can form simple growth twins

94    parallel to (100) (Deer et al. 1982). Two sets of symmetrically equivalent,

95    polysynthetic lamellar mechanical (deformation) twins in titanite were first reported

96    by Mügge (1889), and have since been documented in rocks affected by high-strain

97    rates. Deformation twins were reported in samples affected by 0.5-0.8 GPa pressure

98    during nuclear tests (Borg 1970), and were subsequently produced in laboratory

99    experiments at 0.8 GPa (Borg and Heard 1972). The twin mode for deformation twins

100   was defined as $K_1 = \sim\{221\}$, $\eta_1 = <110>$, where $K_1$ = twinning (or composition) plane

101   and $\eta_1$ = shear direction (Borg 1970). With a critically resolved shear stress of ~0.13

4

102  GPa at 500 °C, ~{221}<110> twinning can occur in titanite at typical endogenic

103  tectono-metamorphic conditions (Borg and Heard 1972; Bonamici et al. 2015).

104      Titanite can also undergo dislocation creep (Müller and Franz 2004; Bonamici

105  et al. 2015) and dynamic recrystallization (Papapavlou et al. 2017) in tectono-

106  metamorphic settings. Crystal-plastic deformation of titanite is not well studied.

107  Dislocations with Burgers vectors (**b**) = [100], [011] and [0$\bar{1}$1] have been reported in

108  titanite at eclogite facies, and easy glide of dislocations with **b** = ½<011> that is

109  predicted to occur in the A2/a phase (Müller and Franz 2004). Recrystallised

110  subgrains with low- and high-angle boundaries have also been reported in

111  tectonically-deformed titanite (Bonamici et al. 2015; Papapavlou et al. 2017; Kirkland

112  et al. 2018).

113      Titanite grains have been experimentally dynamically shocked to 59 GPa

114  (Deutsch and Schärer 1990). However, the resulting microstructures were not

115  characterised in detail. Previously reported titanite microstructures in naturally

116  shocked rocks that did not involve quantitative approaches have been described

117  simply as 'subplanar fractures' (e.g. Koeberl et al. 1996; Papapavlou et al. 2018),

118  'planar fractures' and 'mechanical twinning' (Biren and Spray 2011). In breccia from

119  the Ries crater, Germany, Chao (1968) reported weakly-developed planar features and

120  misoriented mosaic textures. Whereas Abadian (1972) reported dominant cleavage

121  along (111) and (110), less common cleavage in an irrational plane ||(552), and fine

122  (1-2 μm wide) planar elements parallel to the {010} zones. Electron backscatter

123  diffraction analysis of titanite in target rocks from the Sudbury impact structure,

124  Canada, and Vredefort impact structure, South Africa, have been shown to be crystal-

125  plastically deformed, and to contain lamellar twins with ~74° / <102> host-twin

126  disorientation axes, and neoblasts (Papapavlou et al. 2018). However, twins identified

127 in these studies have not been indexed. Until now, no studies have focused on

128 quantitatively distinguishing the style of deformation features that form in titanite in

129 tectonic stress regimes from those that form during impact events, which is the focus

130 of this study.

131

**Geological background and samples**

133 This study investigates titanite from the ~66 Ma, 200 km Chicxulub impact

134 structure in the Gulf of Mexico, which is widely reported to have caused the K-Pg

135 mass extinction (Hildebrand et al. 1991; Schulte et al. 2010; Renne et al. 2013). It is

136 one of the three largest known terrestrial impact structures (Grieve and Therriault

137 2000) and contains a well-preserved peak ring (Fig. 1) (Morgan et al. 1997; Gulick et

138 al. 2008; Gulick et al. 2013; Morgan et al. 2016; Riller et al. 2018). In 2016, IODP-

139 ICDP Expedition 364 drilled core from Hole M0077A (21° 27.009′N, 89° 56.962′W),

140 which penetrated the peak ring (Morgan et al. 2017) (Fig. 1). Recovered lithologies

141 include a section of shocked Paleozoic granitoid basement rocks from depths of 747-

142 1335 meters below sea floor (mbsf) that contain pre-impact mafic and felsic dike

143 lithologies as well as intercalations of impact breccia and impact melt rocks (Fig. 1)

144 (Morgan et al. 2017).

145 The granitic target rocks are coarse-grained and primarily composed of alkali

146 feldspar, quartz, plagioclase, minor biotite, and accessory muscovite, apatite, titanite,

147 epidote, magnetite, ilmenite, and zircon (Gulick et al. 2017; Morgan et al. 2017;

148 Schmieder et al. 2017). Most quartz grains contain multiple decorated planar

149 deformation features (PDFs), planar fractures (PFs), and feather features (FFs) (Fig.

150 2) (e.g. Ferrière et al. 2017; Gulick et al. 2017; Morgan et al. 2017; Rae et al. 2017;

151 Zhao et al. 2017; Rae 2018). Preliminary universal stage (U-stage) analysis of PDF

6

152     orientations in shocked quartz constrains the bulk shock pressure of rocks in the core

153     to ~12 ± 5 to 17 ± 5 GPa (Rae et al. 2017; Feignon et al. 2018; Rae 2018). Titanite

154     grains up to 2 mm long occur as inclusions within all major phases of the granitic

155     rocks, including shocked quartz, and are often spatially associated with and/or include

156     other accessory phases, such as zircon and apatite (Figs. 2, 3).

157

158     **ANALYTICAL METHODS**

159     **Samples and approach used in this study**

160        Titanite grains and associated phases were characterised via optical

161     microscopy, backscattered electron (BSE) imaging, and EBSD mapping in thin

162     sections of three shocked granite core samples from Hole M0077A (364-77-A-121-R-

163     1-75-77, 364-77-A-204-R-1-7-9, and 364-77-A-219-R-1-22-24) from depths of

164     814.85, 1030.00, and 1076.16 metres below sea floor (mbsf), respectively (Figs. 2, 3,

165     and Table 1). The samples are referred to throughout this study by these depths with #

166     prefix (Table 1). Modes of twinning in titanite identified from EBSD data were

167     determined via analysis of the host-twin crystallographic orientation relationships. A

168     MATLAB script was used to determine the directions defining 180° misorientation

169     relationships, which correspond to either the twinning direction of shear ($\eta_1$) or the

170     pole to the compositional plane (twin plane, $K_1$) (Christian and Mahajan 1995;

171     Erickson et al. 2016). Finally, twins were indexed using geometric considerations

172     (Christian and Mahajan 1995) combined with the traces of twin lamellae on EBSD

173     maps. The geometry of low-angle lattice distortions associated with deformation

174     bands seen in EBSD data were analysed, including automated calculation of the

175     weighted Burgers vector (Wheeler et al. 2009).

176

**Scanning electron microscopy and electron backscatter diffraction mapping**

177

178  Prior to scanning electron microscopy, thin sections were polished progressively with

179  diamond paste to 0.5 μm, then given a final polish using 0.06 μm colloidal silica in

180  NaOH on a Buehler Vibromet II for four hours. A thin carbon coat was applied to

181  mitigate charging. Backscattered electron images were collected using a Tescan

182  MIRA3 field emission scanning electron microscope (FE-SEM) in the John de Laeter

183  Centre at Curtin University. Phases and their crystallographic microstructures were

184  quantified using combined energy dispersive X-ray (EDX) and electron backscatter

185  diffraction (EBSD) mapping using an Oxford Instruments AZtec system on the

186  Tescan MIRA3 FE-SEM at Curtin University. Data acquisition settings and

187  processing procedures followed those of Timms et al. (2017b) and are detailed in

188  Table 2. EBSD data were processed using the Tango and Mambo modules of Oxford

189  Instruments Channel 5.10 to produce thematic maps and pole figures, respectively.

190

**Determining twin modes from EBSD data**

191

192      EBSD mapping involves quantification of the crystallographic orientation of

193  phases relative to the sample surface. It is conventional to describe this absolute

194  crystallographic orientation in the x-y-z sample reference frame at a given x-y point

195  on the map as a sequence of three rotations from a reference orientation, known as

196  Euler angles $\phi 1$, $\Phi$, and $\phi 3$ (Bunge 1981; Prior et al. 1999). Twins are recognised in

197  EBSD maps as domains with a specific systematic misorientation relationship relative

198  to the host grain. Misorientation is defined as the rotation around an axis by some

199  angle that would bring any two differently orientated crystals into alignment (Wheeler

200  et al. 2001). Due to the symmetry of crystals, multiple misorientation axes are present.

201  Each axis corresponds to a different angular rotation, and all of these orientations

8

202  describe the relationship between the two domains. The most commonly reported type

203  of misorientation in EBSD data sets is the axis around which the minimum rotation is

204  required for realignment, which is specified as the disorientation (Wheeler et al.

205  2001). This distinction is important when considering mechanical twinning, where it

206  is conventional to classify twin modes based on rotations around axes where the

207  misorientation angle is 180°, and which may be different to the disorientation.

208       Deformation twins are characterized using one or both of the twinning /

209  composition plane, $K_1$, and shear direction, $\eta_1$, which results in 180° misorientation

210  relationships (Christian and Mahajan 1995). Deformation twins can be classified in

211  one of three ways. Type 1 twins have a rational $K_1$, the pole to which is a

212  misorientation axis with rotation angle of 180°, and an irrational $\eta_1$. Conversely, type

213  2 twins have rational $\eta_1$, around which is a misorientation axis with the rotation angle

214  of 180°, and an irrational $K_1$, and compound twins are defined by both rational $K_1$ and

215  $\eta_1$, both of which are misorientation axes with rotations of 180°(Christian and

216  Mahajan 1995). In general, the relationship reported by EBSD software will not have

217  a rotation angle of 180°, as there will usually be a lower angle disorientation

218  relationship. The exceptions to this issue are in triclinic minerals (where there is only

219  one symmetric equivalent) and compound twins in monoclinic minerals (where there

220  are two symmetric equivalents and therefore they must both be components of the

221  twinning). This relationship means it is possible for the disorientation angle/axis to

222  bear no resemblance to $K_1$ and $\eta_1$ for various twin modes in most crystal systems.

223       A more sophisticated analysis of EBSD data that involved calculating 180°

224  misorientations is required to identify $K_1$ and $\eta_1$ for twinning in monoclinic phases

225  such as monazite (Erickson et al. 2016). A MATLAB script was developed that

226  utilizes Euler angle triplets for two representative data points from the host and

9

227 adjacent twin domain derived from the EBSD map, crystal unit cell parameters, and

228 Laue group symmetry operators as input parameters (Table 3).

229    First, the rotation matrix ($\mathbf{R}$), which describes the orientation relative to a

230 reference orientation, is calculated for each Euler triple (host $\mathbf{R_h}$, twin $\mathbf{R_t}$) using

231 equations B2 and B4 of Cho et al. (2005). These can be used to calculate the

232 directions in sample coordinates of particular crystal directions. For our purposes we

233 require a matrix which describes the rotation from host to twin *expressed in crystal*

234 *coordinates* ($\mathbf{R_m} = \mathbf{R_h^{-1}R_t}$). Since this is in crystal coordinates, we derive rotation

235 matrices for each symmetric equivalent ($\mathbf{R_m}$ i = $\mathbf{S_i}$ $\mathbf{R_m}$) where $\mathbf{S_i}$ is the i-th member of

236 the set of symmetry operators for the Laue class under consideration. The 180°

237 misorientation axes were calculated as angle/axis pairs in Cartesian x-y-z coordinates

238 (the sample reference frame). These were used to find best-fit crystallographic forms

239 using the dot product of unit vectors, as <*hkl*> or pole to {*hkl*}, implementing integer

240 search limits of $\bar{4}$ to 4 for *h*, *k*, and *l* to yield low-index (rational) best-fit forms.

241 Output data were compiled giving the crystallographic vector with the smallest value

242 normalised to 1 and their corresponding angular deviation from the calculated

243 misorientation axis. The orientation of $K_1$, $\eta_1$ and S were reconstructed using a

244 stereographic projection, ensuring that the appropriate symmetric variants of $K_1$ and

245 $\eta_1$ were chosen such that its great circle contains the mapped x-y trace of the twins

246 and $\eta_1$.

247    The $K_1$ and $\eta_1$ components of twin modes were deemed to be rational if

248 angular deviation between the calculated misorientation axis and the best-fit low

249 index crystallographic form were <0.7°, which is a reasonable value given the mean

250 angular deviation associated with indexing EBSD data points is typically on the order

251 of 0.3 to 0.8°. Twin mode components were considered irrational where angular

252 deviation to the best-fit low-index form were >0.7° (typically >1.5°). These results

253 were used to classify twin modes as types 1, 2, or compound twins, as described

254 above (Christian and Mahajan 1995). Results are summarized in Tables 4 and 5. For a

255 given twin mode, the disorientation axis is assumed to be defined by the intersection

256 of planes normal to $\eta_1$ for both symmetrically equivalent sets of twins. Therefore, the

257 disorientation axis associated with ~{221} <110> twins (Borg 1970; Borg and Heard

258 1972) is parallel to [102], which is coincident with the pole to (001).

259

**Determination of slip systems**

261       Two approaches were used to determine dislocation slip systems active in

262 shocked titanite. The first approach involved a geometric analysis of crystal-plastic

263 deformation bands using EBSD data, assuming a simple tilt-boundary model, which

264 has been successfully applied to low-angle boundaries in other minerals (Boyle et al.

265 1998; Bestmann and Prior 2003; Reddy et al. 2007). This approach assumes that

266 disorientation axes associated with low-angle deformation bands are a consequence of

267 geometrically necessary dislocations, and that the disorientation axis, pole to the slip

268 plane, and Burgers vector (**b**) are orthonormal. Geometric reconstruction of low-angle

269 tilt boundary planes must contain their traces on EBSD maps and the disorientation

270 axis. The **b** is oriented normal to the tilt boundary, and the slip plane is assumed to

271 contain both **b** and the disorientation axis. The second approach involved automated

272 calculation of the weighted Burgers vector (WBV) of geometrically necessary

273 dislocations using orientation gradients in EBSD data (Wheeler et al. 2009). The

274 WBV is defined as the net Burgers vector of dislocations that intersect an area of the

275 EBSD map, and has been calculated by integration around the edge of a user-defined

276 area.

11

277    In this study, an automated version of the integral approach of Wheeler et al.

278    (2009) was implemented, whereby an EBSD map is automatically tiled into square,

279    20 x 20 pixel (6 x 6 μm) areas, and the WBV calculated for each tile. This method

280    reduces the errors on WBV in comparison to values calculated at every pixel. Results

281    from tiles were disregarded if the square overlapped a high-angle boundary (including

282    twin interfaces) or where the magnitude of the WBV length was below a threshold

283    value (i.e., a minimum dislocation density, ddmin = 0.001 $(\mu m)^{-1}$). The two

284    approaches to deducing dislocation slip systems described above are complementary:

285    the WBV approach is automated and does not involve assumptions about low-angle

286    boundary geometry, whereas the low-angle boundary model also allows indexing of

287    low-angle deformation bands.

288

289    **RESULTS**

290    **Microstructures in Chicxulub Titanite**

291    Four titanite grains were analysed, including a >1 mm long grain in #814.85; a

292    200 μm grain in #1030.00; and two grains from #1076.16 that are 300 μm and 500 μm

293    across, respectively (Figs. 2, 3). The titanite grains occur as inclusions within shocked

294    and fractured alkali feldspar and quartz, and are cut by brittle fractures (Figs. 2-7).

295    None of the studied grains occur in discrete breccia, melt, or cataclasite veins, and are

296    entirely enclosed within granitoid (Fig. 2). Surrounding quartz grains contain multiple

297    sets of PDFs, PFs, FFs (Fig. 2), and high densities of lobate/irregular Dauphiné twins

298    (Figs. 6, 7). Calcite and $TiO_2$ are commonly present along fractures in titanite and

299    along grain boundaries (Figs. 3-7).

300    All titanite grains were indexed as $P2_1/a$, with no evidence of the A2/a

301    structure. All four titanite grains contain two or more sets of polysynthetic twin

12

302  lamellae (Figs. 4-7). Twin lamellae are typically a few micrometres wide, straight to

303  slightly kinked, and tapered. Others terminate against grain boundaries, fractures, or

304  other twins, and are unevenly developed across the grains (Figs. 4-7). In some grains,

305  conspicuous sub-planar partings are present along twin interfaces (e.g., Figs. 4, 5).

306  Each titanite grain contains two sets of twins that are disorientated from the host grain

307  by ~74° / [102] (labelled T1 and T2 in Figs. 4-7). The grain from sample #1030.00

308  contains a third set of twins with a disorientation relative to the host of ~51° / [001]

309  (labelled T3 in Fig. 7A).

310       All host domains in the titanite grains record variable degrees of intragrain

311  misorientation, up to ~30°, which manifests as dispersion in pole figures (Figs. 4-7).

312  While some dispersion is attributed to rigid rotation of fractured blocks, a component

313  is linked to progressive distortion and broad deformation bands with indistinct

314  boundaries, which are the result of crystal-plasticity (e.g., Fig. 5). Significant

315  thickening of twins along deformation bands in titanite grain 1 in #1076.16 indicates

316  that the formation of these microstructures was coeval (Fig. 8). The high angle of the

317  twin planes to the polished surface for this sample (Fig. 8B) means that the true

318  thickness is observed, and the twin thickness is not merely an apparent thickness, due

319  to the plane of observation. The best-developed (strongest and most planar)

320  deformation bands in the analysed titanite grains are defined by systematic

321  crystallographic disorientation about an axis sub-parallel with the pole to {111} (Fig.

322  8A-B). The map traces of the deformation bands are geometrically consistent with

323  low-angle tilt boundaries along {130} that contain the disorientation axis (Fig. 8B).

324  This geometric configuration can be explained by dislocation glide with Burgers

325  vector $\mathbf{b}$ = [341]. This result is supported by weighted Burgers vector analysis, which

13

326      shows WBV forms dominant clusters around [341] (Fig. 8C-E), which has not

327      previously been described in titanite.

328

### Indexing of Twins in Titanite

330      The most common twins encountered in the Chicxulub titanite grains have

331      disorientation relative to the host of ~74° / [102], and 180° misorientation axes that

332      align with <110> of the host grains, which is coincidental with $\eta_1$ of twins described

333      by Borg (1970) (Twins 1 and 2 in Figs. 4-7; Table 5). However, reconstruction of the

334      composition plane ($K_1$) using the map trace of these twins is consistent within a few

335      degrees of $\{\bar{1}11\}$, rather than $\{221\}$ expected for Borg (1970) twins. Therefore, they

336      define two symmetric equivalents of a previously undescribed type 2 twin mode with

337      $K_1$, = irrational $\sim\{\bar{1}11\}$, $\eta_1$ = rational <110>, and shear plane (S) = {112} (Fig. 10,

338      Table 5). A geometric consequence of this host-twin orientation relationship is that it

339      results in coincidence of many crystallographic planes between twin and host that lie

340      normal to $\eta_1$ <110>, the 180° misorientation axis (Figs. 4-7, Table 5).

341      Twins with ~51° / [001] disorientation were found in one grain (labelled T3 in

342      Fig. 7A). The 180° misorientation axis for these twins aligns with the pole to {130},

343      which defines a previously undescribed twin mode $K_1$ = {130}, $\eta_1$ = irrational

344      $\sim$<522>, and S = $(10\bar{3})$ (Table 5; Fig. 7B, 10). Two symmetrically equivalent variants

345      are possible for this twin mode, which are classified as type 1 twins because they have

346      a rational $K_1$ (Christian and Mahajan 1995) (Fig. 10).

347      Distinguishing between the newly described type 2 $\sim\{\bar{1}11\}$ twins and the

348      established $\sim\{221\}$ twins requires care, because they have identical $\eta_1$ (parallel to

349      <110>) and thus produce identical disorientation axis/angle relationships using EBSD

350      data (Fig. 10, Table 5). Therefore, correct indexing requires consideration of the trace

351 of twin planes on the EBSD map and $\eta_1$ to reconstruct $K_1$ (e.g., Figs. 4-7). Indexing of

352 the newly described type 1 {130} ~<522> twins is straightforward because it can be

353 inferred from the disorientation angle/axis alone, as no other twins are known to have

354 similar relationships.

355

**Microstructures in Co-existing Zircon**

357      A total of eight zircon grains were analysed in the same thin sections as the

358 titanite grains, including zircon grains that occur as inclusions within the larger

359 shocked titanite grains (Fig 3A). The zircon grains are typically <60 μm across,

360 euhedral to anhedral in shape, with some grains preserving evidence of growth

361 zoning. All of the grains are fractured, and most of the observed variations in

362 crystallographic orientation, shown by variations in colour in EBSD orientation maps

363 and pole figures in Fig. 9, are related to rotation of rigid blocks separated by fractures

364 (Fig. 9A, B, D, F, and G). However, the zircon grains preserve minor evidence (<5°)

365 of crystal-plastic strain, seen as smooth, systematic gradients in orientation that are

366 not related to fractures (Fig. 9A, E, and H). No microstructures diagnostic of shock

367 metamorphism, such as {112} twins, the high-pressure polymorph reidite, granular

368 neoblasts, or dissociation textures (e.g. Timms et al. 2017b), were detected in the

369 zircon grains analysed. If present, these microstructures would have been readily

370 detected by the EBSD analysis utilized in this study.

371

**DISCUSSION**

**New titanite twins in Chicxulub shocked granite**

374      The two twin types found in Chicxulub titanite described here have not been

375 reported previously in tectonically-deformed titanite, and we propose that they are a

376    product of shock metamorphism during hypervelocity impact conditions given the

377    occurrence in granitoid with well-documented quartz microstructures indicative of

378    shock pressures of about 12 to 17 GPa. Thus, our results offer new insights into how

379    titanite deforms in impact environments. The new twin modes are geometrically

380    distinct from previously established mechanical and/or growth twins in titanite (e.g.

381    Borg 1970) (Fig. 10, Tables 4 and 5). The most common twins in Chicxulub titanite

382    grains have irrational composition planes ($K_1$) that are within a few degrees of $\{\bar{1}11\}$,

383    and a rational $\eta_1 = <110>$, and (S) = $\{112\}$. Chicxulub titanite grains typically have

384    two sets of $\sim\{\bar{1}11\} <110>$ twins, which is the maximum number possible given the

385    monoclinic symmetry. One unusual aspect of $\sim\{\bar{1}11\} <110>$ twins is that they share

386    an identical twin-host minimum misorientation (disorientation) relationship with

387    previously established $\sim\{221\} <110>$ twins (e.g., Borg, 1970), and thus the two twin

388    types cannot be distinguished solely based on disorientation angle/axis measurements

389    provided by EBSD analysis. Identification of each twin type thus requires indexing of

390    the composition planes (twin planes), which we calculated using a MATLAB script.

391          A set of lamellar twins with a different host-twin disorientation

392    crystallographic relationship of $\sim51° / [001]$ was found in one Chicxulub grain

393    (labelled T3 in Fig. 2A). These twins represent a second previously undescribed twin

394    mode in titanite, whereby $K_1 = \{130\}$, $\eta_1 =$ irrational $\sim<522>$, and S = $(10\bar{3})$ (Table

395    4; Fig. 7B, 9C). Indexing of the newly described $\{130\} \sim<522>$ twins is

396    straightforward because it can be inferred from the disorientation angle/axis relations

397    provided by EBSD data.

398

399    **Concurrent deformation processes in titanite during shock metamorphism**

16

400       The thickening of ~$\{\bar{1}11\}$ <110> mechanical twins along {130} deformation

401    bands clearly indicates that dislocations with **b** [341] occurred concurrently with

402    twinning (Fig. 8). Concurrent crystal-plasticity could potentially have affected

403    twinning in two different ways: (1) the widening of twins was mechanically

404    facilitated by $\{\bar{1}12\}$ [341] dislocation activity, and/or (2) the formation of

405    deformation bands locally re-orientated titanite into a more favourable orientation for

406    twinning with respect to the stress field of the shock wave. Given that the slip vector

407    for twinning and Burgers vector for dislocation glide are similarly-oriented (i.e.,

408    twinning $\eta_1$ = <110> and dislocation **b** = <341>, respectively, are within ~10° of one

409    another), it is possible that these two types of microstructure have accommodated

410    shock deformation in a coherent and systematic way similar to cross slip. However,

411    the effects of localised re-orientation in deformation bands on the ease of twinning

412    cannot be resolved without additional information about the nature of the stress-strain

413    field associated with the passing shock wave relative to the orientation of the grains

414    and critically-resolved shear stress for twinning. Nevertheless, the absence of {130}

415    deformation bands in other shock-twinned grains in this study indicates that

416    concurrent [341] dislocation slip is not a requirement for these twin modes in titanite.

417

**418    Petrological implications of the new twin modes in titanite**

419       Titanite in the target rocks that formed the peak ring at the Chicxulub crater

420    responded to the ~12–17 GPa bulk peak shock pressure principally by ~$\{\bar{1}11\}$ <110>

421    twinning, with minor {130} ~<522> twinning and coeval crystal-plasticity. Zircon, a

422    tetragonal accessory phase, is also known to form deformation twins and other

423    microstructures during shock deformation (Fig. 11). In contrast to titanite, zircon

424    grains in the same samples do not record diagnostic shock/impact-related

425 microstructures (Fig. 9), which is consistent with their having experienced shock

426 pressure <20 GPa (e.g. Timms et al. 2017b). In this respect, titanite appears similar to

427 xenotime, which has also been shown by empirical calibration with quartz and zircon

428 to form impact-related deformation twins and plastic deformation at shock pressures

429 <20 GPa (Cavosie et al. 2016b) (Fig. 11). Differences in the response of titanite and

430 other accessory minerals to shock deformation are shown in Fig. 11. The variable

431 microstructural responses are presumably related to the intrinsic material properties of

432 the different minerals, such as elasticity and yield strength for various failure modes,

433 which are largely controlled by crystal structure. Phase transformations and reactions

434 that determine phase stability through shock conditions are also important.

435     The precise details of the kinetics, nucleation stress, and critically resolved

436 shear stress for the newly described twin modes are yet to be determined by

437 theoretical or experimental means. However, unlike for shock twinning and

438 dislocations in zircon (Timms et al. 2018), theoretical calculations are inhibited by the

439 current lack of published elastic constants for $P2_1/a$ titanite. More rigorous

440 investigations into the shock response of titanite via laboratory shock deformation

441 experiments remain an avenue for future research. Furthermore, very few quantitative

442 microstructural studies of naturally deformed titanite from tectonic and/or impact

443 environments are currently available (Papapavlou et al. 2017; Papapavlou et al. 2018).

444 Thus, further studies of naturally shocked and tectonically-deformed titanite are

445 required to provide better constraints on formation conditions for different twin

446 modes.

447     The discovery of new titanite twin modes in shocked target rocks at Chicxulub

448 represents the first steps toward developing a twin-based framework for using titanite

449 to distinguish tectonic versus impact-related deformation, similar to the approach

18

450  developed recently for monazite (Erickson et al. 2016). Titanite appears to behave

451  similarly to monazite in that a range of twin modes have been reported, with empirical

452  studies indicating that certain twin types uniquely form as a consequence of shock

453  deformation. Cleavage along ~$\{\bar{1}11\}$ twin planes shown by several of the Chicxulub

454  grains is different to the dominant cleavage orientations reported for titanite from the

455  Ries crater (Abadian 1972). If titanite commonly cleaves along twin lamellae, then

456  observations of cleavage made by Abadian (1972) may be an indication that

457  additional shock twin modes could be revealed via detailed studies of shocked titanite

458  from other impact structures (Papapavlou et al. 2018). Our findings further indicate

459  that additional information is required to singular twin disorientation axes produced

460  from EBSD data in order to correctly index twins in titanite.

461

462  **Broader applications of deformation twin systematics**

463       In this study, we outline an approach for rigorous indexing and classification

464  of deformation twins from EBSD data based on geometric considerations of Christian

465  and Mahajan (1995). We demonstrate the importance of our approach for

466  distinguishing twin modes in titanite formed in tectonic versus shock settings. This

467  approach builds on the method outlined by Erickson et al. (2016) that led to the

468  discovery of new twin modes in monazite, and can be applied to other minerals that

469  form twins, such as ilmenite, rutile, and pyrrhotite, which could be useful for better

470  understanding deformation of rocks in both tectonic and impact settings.

471

472  **CONCLUSIONS**

473       In conclusion, titanite is a common accessory phase in a variety of rock types

474  (Frost et al. 2001), which has the propensity to record impact-related microstructures.

475 Specifically, we demonstrate titanite undergoes shock-related deformation twinning

476 along ~$\{\bar{1}11\}$ and $\{130\}$, as recorded in the shocked target rocks of the Chicxulub

477 impact structure over the pressure range between $12 \pm 5$ and $\sim17 \pm 5$ GPa. These twin

478 modes can form concurrently with deformation bands along $\{130\}$ resulting from

479 dislocation migration with a <341> Burgers vector. The newly-described twin modes

480 in ~$\{\bar{1}11\}$ and $\{130\}$ are different from previously reported ~$\{221\}$ twins from

481 tectonically-deformed titanite, and we therefore hypothesize that they are indicative of

482 shock conditions. We have defined geometric criteria for distinguishing these various

483 twins in titanite, which highlights the importance of utilizing a rigorous approach for

484 indexing twins. Furthermore, as this accessory mineral may be susceptible to age-

485 resetting during deformation (Papapavlou et al. 2017; Papapavlou et al. 2018), we

486 propose that our findings greatly increase the potential of titanite as a diagnostic

487 recorder of impact events in the geological record.

488

505

506 **FIGURE CAPTIONS**

507 **Figure 1.** A. Gravity anomaly map of the Chicxulub impact structure showing traces

508 of various morphological features of the buried crater (dashed lines), location of Hole

509 M0077A, and sinkholes (cenotes) (white dots), and present-day coastline (solid white

510 line). B. Schematic core log of Hole M0077A showing the distribution of lithologies

511 and locations of samples used in this study. After Morgan et al. (2016) and Gulick et

512 al. (2013).

513

514 **Figure 2**. Optical photomicrographs of the samples used in this study. Mineral

515 abbreviations after Whitney and Evans (2009) include: Qz = quartz; Afs = alkali

516 feldspar; Pl = plagioclase; Ttn = titanite; Chl = chlorite; Bt = biotite. A. #814.85. B.

517 #1030.00. C. #1076.16. D. Region of interest in #1076.16 shown by white box in C.

518 White arrows annotate significant fracture orientations. Samples were impregnated

519 with blue epoxy prior to thin sectioning to enable the porosity to be visualized. Plane

520 polarized light images.

521

522 **Figure 3**. Backscattered electron images of titanite grains. Mineral abbreviations after

523 Whitney and Evans (2009) include: Qz = quartz; Afs = alkali feldspar; Pl =

524 plagioclase; Ttn = titanite; Zrn = zircon; Cal = calcite; Ap = apatite; Mag = magnetite;

525    Bt = biotite; Hc = hercynite. A. K-feldspar-hosted titanite in #814.85 shown in Fig.

526    2A. B. Detail of the margin of the titanite grain in A, showing a fractured zircon grain

527    and five sets of planar microstructures in alkali feldspar (black arrows). C. Primary

528    titanite, magnetite and apatite in a quartz domain in #1030.00 shown in Fig. 2B. D.

529    Apatite grains with planar fractures in an alkali feldspar domain in #1030.00. E.

530    Titanite in an alkali feldspar domain in #1076.16 shown in Fig. 2C. F. Titanite with

531    apatite, magnetite, zircon and hercynite in a quartz domain in #1076.16 shown in Fig.

532    2D. White arrows in A-F indicate the trace of transgranular fractures.

533

534    **Figure 4**. Microstructure of titanite grain from #814.85 (Fig. 3A). A. Cumulative

535    disorientation map showing 30° variation across the grain and two sets of twins

536    (labelled T1 and T2). An inclusion of a titanite grain with a different orientation is

537    shown by white outline labelled (i). B-C. Detailed maps of region shown in A. D.

538    Pole figures for (100), (010) and (001). Lower hemisphere, equal area projections in

539    the sample x-y-z reference frame. E. Crystallographic relationships between twin and

540    host for twins shown in A-C in the sample reference frame.

541

542    **Figure 5.** Microstructure of titanite grain 1 from #1076.16 (Fig. 3E). A. Cumulative

543    disorientation map showing 20° variation across the titanite grain and two sets of

544    twins (labelled T1 and T2). Fractures and perthitic lamellae are present in surrounding

545    K-feldspar grains. Inset (i) is a detailed map showing T2 twins. B. Pole figures for

546    (100), (010) and (001). Sparse systematically misindexed points at host-twin

547    interfaces (labelled as 's.m.') have disorientation relationships of 98° / $<\overline{2}\overline{1}2>$ and

548    180° / [003]. Lower hemisphere, equal area projections in the sample x-y-z reference

549  frame. C. Crystallographic relationships between twin and host for twins shown in A

550  in the sample reference frame.

551

552  **Figure 6**. Microstructure of titanite grain 2 from #1076.16 (Fig. 3F). A. Cumulative

553  disorientation map showing 30° variation across the titanite grain and two sets of

554  twins (labelled T1 and T2). Dauphiné twins are present in surrounding quartz grains,

555  and magnetite contains thin lamellar twins. Inset (i) is a detailed map showing T2

556  twins. B. Pole figures for (100), (010) and (001). Lower hemisphere, equal area

557  projections in the sample x-y-z reference frame. C. Crystallographic relationships

558  between twin and host for twins shown in A in the sample reference frame.

559

560  **Figure 7.** A. EBSD map of titanite in sample #1030.00 from the Chicxulub crater

561  peak ring (Fig. 3C). Titanite is coloured for cumulative disorientation relative to

562  reference orientation (red cross) and has three sets of twins (T1, T2, and T3). It is

563  surrounded by quartz with Dauphiné twins (Qz, orange/red), calcite (Cal, yellow) and

564  $TiO_2$. Inset (i) shows pole figure for (100) in sample reference frame. B.

565  Crystallographic relationships between twins T1, T2, and T3 and host grain. Several

566  low-index poles to coincident planes (grey circles) align along the plane normal to $\eta_1$

567  for Twins 1 and 2. Lower hemisphere, equal area projections in the sample x-y-z

568  reference frame.

569

570  **Figure 8.** A. Detailed EBSD map of grain 1 from #1076.16 shown in Fig. 5. Titanite

571  is coloured for cumulative disorientation relative to reference orientation (red cross)

572  and twins (purple, labelled T1). Crystal-plastic deformation band (green-orange

573  domain) has a well-defined lower boundary trace (white dashed line), and is displaced

23

574    by brittle fractures. Twin lamellae are thicker within the deformation band. B.

575    Composite pole figure of data shown by the white box in A, plotted in the sample x-y-

576    z reference frame. Crystallographic data show a systematic dispersion about a

577    disorientation axis approximately parallel to the pole to (111). The deformation band

578    is consistent with a (130) tilt boundary geometry that contains the disorientation axis

579    and the trend of the deformation band on the polished surface. The dominant

580    dislocation slip system that contributed to the deformation bands involved glide with

581    a [341] Burgers vector. C EBSD map of the entire grain showing results of automated

582    weighted Burgers vector (WBV) analysis. Superimposed squares indicate 6 x 6 μm

583    tiles from which the integral WBV was calculated. Tiles that overlap with twin

584    domains have been disregarded. Tiles are coloured for WBV orientation using an

585    inverted pole figure (IPF) colour scheme. D Pole figure of WBV data shown in C,

586    plotted in crystallographic reference frame. E Contoured pole figure of data shown in

587    D, indicating dominance of WBV parallel to [341].

588

589    **Figure 9**. Microstructure of zircon grains associated with titanite from samples

590    #814.85 and #1030.00 of this study.

591

592    **Figure 10**. Summary of the geometric elements of deformation microstructures in

593    titanite. Pole Figures A. ~{221} <110> twins after Borg (1970). B. ~{$\bar{1}$11} <110>

594    twins, this study. C. {130} ~<522> twins, this study. D. {130} deformation bands,

595    this study. The two possible symmetric equivalent variants are shown for each type of

596    microstructure. Microstructures shown in B, C, and D have not been described from

597    tectonically-deformed titanite.

598

599 **Figure 11**. Accessory phases as indicators of shock metamorphism. [1]: Leroux et al.

600 (1999), [2]: Timms et al. (2012), [3]: Moser et al. (2009), [4]: Timms et al. (2017a),

601 [5]: Erickson et al. (2013), [6]: Nemchin et al. (2009), [7]: Timms et al. (2018), [8]:

602 Moser et al. (2011), [9]: Thomson et al. (2014), [10]: Cox et al. (2018), [11]:

603 Wittmann et al. (2006), [12]: Cavosie et al. (2015b), [13]: Reddy et al. (2015), [14]:

604 Erickson et al. (2017a), [15]: Cavosie et al. (2015a), [16]: Cavosie et al. (2016a), [17]:

605 Cavosie et al. (2018b), [18]: Timms et al. (2017b), [19]: Erickson et al. (2015), [20]:

606 Erickson et al. (2016), [21]: Erickson et al. (2017b), [22]: Cavosie et al. (2016b), [23]:

607 Darling et al. (2016), [24]: White et al. (2018), [25]: Müller and Franz (2004), [26]:

608 Borg (1970), [27]: Papapavlou et al. (2018), [28]: Papapavlou et al. (2017). Note that

609 the pressures indicated are specifically mean (bulk) pressures for rocks with

610 negligible initial porosity, such as the granitoids in this study. The effects of porosity

611 on bulk shock pressure have been treated elsewhere (e.g., Güldemeister et al. 2013).

612

613

614

615 **\* IODP-ICDP Expedition 364 Scientists**

616 S. P. S. Gulick[1], J. V. Morgan[2], E. Chenot[3], G. L. Christeson[4], P. Claeys[5], C. S.

617 Cockell[6], M. J. L. Coolen[7], L. Ferrière[8], C. Gebhardt[9], K. Goto[10], S. Green[11], H.

618 Jones[12], D. A. Kring[13], J. Lofi[3], C. M. Lowery[4], R. Ocampo-Torres[14], L. Perez-Cruz[15],

619 A. E. Pickersgill[16, 17], M. H. Poelchau[18], A. S. P. Rae[2, 18], C. Rasmussen[4,19], M.

620 Rebolledo-Vieyra[20], U. Riller[21], H. Sato[22], J. Smit[23], S. M. Tikoo[24], N. Tomioka[25], J.

621 Urrutia-Fucugauchi[15], M. T. Whalen[26], A. Wittmann[27], L. Xiao[28], K. E. Yamaguchi[29,

622 30].

623 [1]Institute for Geophysics and Department of Geological Sciences, Jackson School of

624 Geosciences, University of Texas at Austin, Austin, TX, USA. [2]Department of Earth

625 Science and Engineering, Imperial College London, London, UK. [3] Géosciences

626 Montpellier, Université de Montpellier, Montpellier, France. [4]Institute for

627 Geophysics, Jackson School of Geosciences, University of Texas at Austin, Austin,

628 TX, USA. [5]Analytical, Environmental and Geo-Chemistry, Vrije Universiteit Brussel,

629 Brussels, Belgium. [6]Centre for Astrobiology, School of Physics and Astronomy,

630 University of Edinburgh, Edinburgh, UK. [7]Department of Chemistry, WA-Organic

631 and Isotope Geochemistry Centre, Curtin University, Perth, Western Australia,

632 Australia. [8]Natural History Museum, Vienna, Austria. [9]Alfred Wegener Institute

633 Helmholtz Centre of Polar and Marine Research, Bremerhaven, Germany.

634 [10]International Research Institute of Disaster Science, Tohoku University, Sendai,

635 Japan. [11]British Geological Survey, Edinburgh, UK. [12]Department of Geo sciences,

636 Pennsylvania State University, University Park, PA, USA. [13]Lunar and Planetary

637 Institute, Houston, TX, USA. [14]Groupe de Physico-Chimie de l'Atmosphère, L'Institut

638 de Chimie et Procédés pour l'Énergie, l'Environnement et la Santé (ICPEES),

639 Université de Strasbourg, Strasbourg, France. [15]Instituto de Geofísica, Universidad

640 Nacional Autónoma De México, Mexico, Mexico. [16]School of Geographical and Earth

641 Sciences, University of Glasgow, Glasgow, UK. [17]Argon Isotope Facility, Scottish

642 Universities Environmental Research Centre, East Kilbride, UK. [18]Institut für Geo-

643 und Umweltnaturwissenschaften, Albert-Ludwigs-Universität, Freiburg, Germany.

644 [19]Department of Geology and Geophysics, University of Utah, Salt Lake City, UT,

645 USA. [20]Independent consultant, Cancun, Mexico. [21]Institut für Geologie, Universität

646 Hamburg, Hamburg, Germany. [22]Japan Agency for Marine-Earth Science and

647 Technology, Kanagawa, Japan. [23]Faculty of Earth and Life Sciences (FALW), Vrije

26

648 *Universiteit Amsterdam, Amsterdam, Netherlands.* [24]*Earth and Planetary Sciences,*

649 *Rutgers University, New Brunswick, NJ, USA.* [25]*Kochi Institute for Core Sample*

650 *Research, Japan Agency for Marine-Earth Science and Technology, Kochi, Japan.*

651 [26]*Department of Geosciences, University of Alaska Fairbanks, Fairbanks, AK, USA.*

652 [27]*Eyring Materials Center, Arizona State University, Tempe, AZ, USA.* [28]*School of*

653 *Earth Sciences, Planetary Science Institute, China University of Geosciences, Wuhan,*

654 *China.* [29]*Department of Chemistry, Toho University, Chiba, Japan.* [30]*NASA*

655 *Astrobiology Institute.*

656

**657 REFERENCES CITED**

658

659

660 Abadian M (1972) Petrography, shock metamorphism and genesis of polymict

661 cristalline breccias in the Nordlinger Ries. Contributions to Mineralogy and Petrology

662 35(3):245

663 Angel RJ, Kunz M, Miletich R, Woodland AB, Koch M, Xirouchakis D (1999) High-

664 pressure phase transition in $CaTiOSiO_4$ titanite. Phase Transitions 68(3):533-543

665 doi:10.1080/01411599908224532

666 Bestmann M, Prior DJ (2003) Intragranular dynamic recrystallization in naturally

667 deformed calcite marble: diffusion accommodated grain boundary sliding as a result

668 of subgrain rotation recrystallization. Journal of Structural Geology 25(10):1597-1613

669 doi:10.1016/s0191-8141(03)00006-3

670 Biren MB, Spray JG (2011) Shock veins in the central uplift of the Manicouagan

671 impact structure: Context and genesis. Earth and Planetary Science Letters 303(3-

672 4):310-322 doi:10.1016/j.epsl.2011.01.003

673 Bonamici CE, Fanning CM, Kozdon R, Fournelle JH, Valley JW (2015) Combined

674 oxygen-isotope and U-Pb zoning studies of titanite: New criteria for age preservation.

675 Chemical Geology 398:70-84 doi:10.1016/j.chemgeo.2015.02.002

676 Borg IY (1970) Mechanical <110> twinning in shocked sphene. American

677 Mineralogist 55:1876-1888

678 Borg IY, Heard HC (1972) Mechanical twinning in sphene at 8 Kbar, 25° to 500° C.

679 Geological Society of America Memoirs 132:585-592

680 Boyle AP, Prior DJ, Banham MH, Timms NE (1998) Plastic deformation of

681 metamorphic pyrite: new evidence from electron-backscatter diffraction and

682 forescatter orientation-contrast imaging. Mineralium Deposita 34(1):71-81

683 doi:10.1007/s001260050186

684 Bunge HJ (1981) Fabric analysis by orientation distribution functions.

685 Tectonophysics 78(1-4):1-21

686 Cavosie AJ, Erickson TM, Timms NE, Reddy SM, Talavera C, Montalvo SD, Pincus

687 MR, Gibbon RJ, Moser D (2015a) A terrestrial perspective on using ex situ shocked

688 zircons to date lunar impacts. Geology 43(11):999-1002 doi:10.1130/g37059.1

689 Cavosie AJ, Erickson TM, Timms NE (2015b) Nanoscale records of ancient shock

690 deformation: Reidite ($ZrSiO_4$) in sandstone at the Ordovician Rock Elm impact crater.

691 Geology 43(4):315-318 doi:10.1130/g36489.1

692 Cavosie AJ, Timms NE, Erickson TM, Hagerty JJ, Hörz F (2016a) Transformations

693 to granular zircon revealed: Twinning, reidite, and $ZrO_2$ in shocked zircon from

694 Meteor Crater. Geology 44(9):703-706

695 Cavosie AJ, Montalvo PE, Timms NE, Reddy SM (2016b) Nanoscale deformation

696 twinning in xenotime, a new shocked mineral, from the Santa Fe impact structure

697 (New Mexico, USA). Geology 44(10):803-806

698   Cavosie AJ, Timms NE, Erickson TM, Koeberl C (2018a) New clues from Earth's

699   most elusive impact crater: Evidence of reidite in Australasian tektites from Thailand.

700   Geology  doi:10.1130/g39711.1

701   Cavosie AJ, Timms NE, Ferrière L, Rochette P (2018b) FRIGN zircon—The only

702   terrestrial mineral diagnostic of high‑pressure and high‑temperature shock

703   deformation. Geology 46(10):891-894 doi:10.1130/G45079.1

704   Chao ECT (1968) Pressure and temperature histories of impact metamorphosed

705   rocks—based on petrographic observations. In: French BM, Short NM (eds) Shock

706   metamorphism of natural materials, vol. Mono Press, Baltimore, Md, pp 135-158

707   Cho JH, Rollett AD, Oh KH (2005) Determination of a mean orientation in electron

708   backscatter diffraction measurements. Metallurgical and Materials Transactions A

709   36(12):3427-3438

710   Christian JW, Mahajan S (1995) Deformation twinning. Progress in Materials Science

711   39:1-57

712   Cox MA, Cavosie AJ, Bland PA, Miljković K, Wingate MTD (2018) Microstructural

713   dynamics of central uplifts: Reidite offset by zircon twins at the Woodleigh impact

714   structure, Australia. Geology  doi:10.1130/g45127.1

715   Crow CA, Moser DE, McKeegan KD (2018) Shock metamorphic history of >4 Ga

716   Apollo 14 and 15 zircons. Meteoritics & Planetary Science  doi:10.1111/maps.13184

717   Darling JR, Moser DE, Barker IR, Tait KT, Chamberlain KR, Schmitt AK, Hyde BC

718   (2016) Variable microstructural response of baddeleyite to shock metamorphism in

719   young basaltic shergottite NWA 5298 and improved U–Pb dating of Solar System

720   events. Earth and Planetary Science Letters 444:1-12 doi:10.1016/j.epsl.2016.03.032

721   Deer WA, Howie RA, Zussman J (1982) Rock-Forming Minerals: Orthosilicates,

722   Volume 1A (2nd Edition). Geological Society of London,

723 Deutsch A, Schärer U (1990) Isotope systematics and shock-wave metamorphism: I.

724 U-Pb in zircon, titanite and monazite, shocked experimentally up to 59 GPa.

725 Geochimica et Cosmochimica Acta 54(12):3427-3434

726 Erickson TM, Cavosie AJ, Moser DE, Barker IR, Radovan HA (2013) Correlating

727 planar microstructures in shocked zircon from the Vredefort Dome at multiple scales:

728 Crystallographic modeling, external and internal imaging, and EBSD structural

729 analysis. American Mineralogist 98(1):53-65 doi:10.2138/am.2013.4165

730 Erickson TM, Pearce MA, Taylor RJM, Timms NE, Clark C, Reddy SM, Buick IS

731 (2015) Deformed monazite yields high-temperature tectonic ages. Geology 43(5):383-

732 386 doi:10.1130/g36533.1

733 Erickson TM, Cavosie AJ, Pearce MA, Timms NE, Reddy SM (2016) Empirical

734 constraints on shock features in monazite using shocked zircon inclusions. Geology

735 44(8):635-638

736 Erickson TM, Pearce MA, Reddy SM, Timms NE, Cavosie AJ, Bourdet J, Rickard

737 WDA, Nemchin AA (2017a) Microstructural constraints on the mechanisms of the

738 transformation to reidite in naturally shocked zircon. Contributions to Mineralogy and

739 Petrology 172(1):6

740 Erickson TM, Timms NE, Kirkland CL, Tohver E, Cavosie AJ, Pearce MA, Reddy

741 SM (2017b) Shocked monazite chronometry: integrating microstructural and *in situ*

742 isotopic age data for determining precise impact ages. Contributions to Mineralogy

743 and Petrology 172(2-3):11 doi:10.1007/s00410-017-1328-2

744 Feignon J-G, Ferrière L, Koeberl C (2018) Petrography and shock metamorphism of

745 granitoid samples from the Chicxulub peak-ring IODP-ICDP expedition 364 drill

746 core. EGU General Assembly Conference Abstracts 20

747  Ferrière L, Rae ASP, Poelchau M, Koeberl C, Party atI-IES (2017) Macro- and

748  microscopic evidence of impact metamorphism in rocks from the Chicxulub peak ring

749  IODP-ICDP Expedition 364 drill core. In: 48th Lunar and Planetary Science

750  Conference, vol., The Woodlands, Texas, p 1600

751  Frost BR, Chamberlain KR, Schumacher JC (2001) Sphene (titanite): phase relations

752  and role as a geochronometer. Chemical Geology 172(1-2):131-148

753  Grieve R, Therriault A (2000) Vredefort, Sudbury, Chicxulub: three of a kind?

754  Annual Review of Earth and Planetary Sciences 28(1):305-338

755  Güldemeister N, Wünnemann K, Durr N, Hiermaier S (2013) Propagation of impact-

756  induced shock waves in porous sandstone using mesoscale modeling. Meteoritics &

757  Planetary Science 48(1):115-133 doi:10.1111/j.1945-5100.2012.01430.x

758  Gulick S, Morgan J, Mellett CL, Green SL, Bralower T, Chenot E, Christeson G,

759  Claeys P, Cockell C, Coolen MJL, Ferrière L, Gebhardt C, Goto K, Jones H, Kring D,

760  Lofi J, Lowery C, Ocampo-Torres R, Perez-Cruz L, Pickersgill AE, Poelchau M, Rae

761  A, Rasmussen C, Rebolledo-Vieyra M, Riller U, Sato H, Smit J, Tikoo S, Tomioka N,

762  Urrutia-Fucugauchi J, Whalen M, Wittmann A, Yamaguchi K, Xiao L, Zylberman W

763  (2017) Expedition 364 summary. In: Morgan J, Gulick S, Mellett CL, Green SL,

764  Scientists atE eds) Proceedings of the International Ocean Discovery Program, vol

765  364. College Station, TX (International Ocean Discovery Program), Texas, pp 1-23

766  Gulick SP, Barton PJ, Christeson GL, Morgan JV, McDonald M, Mendoza-Cervantes

767  K, Pearson ZF, Surendra A, Urrutia-Fucugauchi J, Vermeesch PM, Warner MR

768  (2008) Importance of pre-impact crustal structure for the asymmetry of the Chicxulub

769  impact crater. Nature Geoscience 1(2):131

770  Gulick SPS, Christeson GL, Barton PJ, Grieve RAF, Morgan JV, Urrutia-Fucugauchi

771  J (2013) Geophysical characterization of the Chicxulub impact crater. Reviews of

772  Geophysics 51(1):31-52 doi:10.1002/rog.20007

773  Hayward PJ, Cecchetto EV (1982) Scientific Basis for Nuclear Waste Management.

774  North Holland, Amsterdam

775  Hey MH (1982) International Mineralogical Association: commission on new

776  minerals and mineral names. Mineralogical Magazine 46(341):513-514

777  Higgins JB, Ribbe PH (1976) The crystal chemistry and space groups of natural and

778  synthetic titanites. American Mineralogist 61(9-10):878-888

779  Hildebrand AR, Penfield GT, Kring DA, Pilkington M, Camargo Z A, Jacobsen SB,

780  Boynton WV (1991) Chicxulub crater: a possible Cretaceous/Tertiary boundary

781  impact crater on the Yucatan Peninsula, Mexico. Geology 19(9):867-871

782  Kirkland CL, Fougerouse D, Reddy SM, Hollis J, Saxey DW (2018) Assessing the

783  mechanisms of common Pb incorporation into titanite. Chemical Geology 483:558-

784  566 doi:10.1016/j.chemgeo.2018.03.026

785  Koeberl C, Reimold WU, Kracher A, Träxler B, Vormaier A, Körner W (1996)

786  Mineralogical, petrological, and geochemical studies of drill core samples from the

787  Manson impact structure, Iowa. Geological Society of America Special Papers

788  302(166)

789  Kunz M, Xirouchakis D, Lindsley DH, Hausermann D (1996) High-pressure phase

790  transition in titanite ($CaTiOSiO_4$). American Mineralogist 81(11-12):1527-1530

791  Leroux H, Reimold WU, Koerberl C, Hornemann U, Doukan J-C (1999)

792  Experimental shock deformation in zircon: a transmission electron microscopy study.

793  Earth and Planetary Science Letters 169:291-301

794  Morgan J, Warner M, Brittan J, Buffler R, Camargo A, Christeson G, Denton P,

795  Hildebrand A, Hobbs R, Macintyre H, Mackenzie G (1997) Size and morphology of

796  the Chicxulub impact crater. Nature 390(6659):472

797  Morgan J, Gulick S, Mellett CL, Green SL, Expedition364Scientists (2017)

798  Chicxulub: Drilling the K-Pg Impact Crater. Expedition 364 of the mission-specific

799  drilling platform from and to Progresso, Mexico. Site M0077. Proceedings of the

800  International Ocean Discovery Program 364

801  Morgan JV, Gulick SP, Bralower T, Chenot E, Christeson G, Claeys P, Cockell C,

802  Collins GS, Coolen MJ, Ferrière L, Gebhardt C (2016) The formation of peak rings in

803  large impact craters. Science 354(6314):878-882

804  Moser DE, Davis WJ, Reddy SM, Flemming RL, Hart RJ (2009) Zircon U–Pb strain

805  chronometry reveals deep impact-triggered flow. Earth and Planetary Science Letters

806  277(1-2):73-79 doi:10.1016/j.epsl.2008.09.036

807  Moser DE, Cupelli CL, Barker IR, Flowers RM, Bowman JR, Wooden J, Hart JR

808  (2011) New zircon shock phenomena and their use for dating and reconstruction of

809  large impact structures revealed by electron nanobeam (EBSD, CL, EDS) and isotopic

810  U–Pb and (U–Th)/He analysis of the Vredefort dome. Canadian Journal of Earth

811  Sciences 48(2):117-139 doi:10.1139/e11-011

812  Mügge O (1889) Über durch Druck entstandene Zwillinge von Titanit nach den

813  Kanten [110] und [HO]. , 11, 98. Neues Jahrb Mineral, Geologie u Paläontologie

814  11:98-115

815  Müller WF, Franz G (2004) Unusual deformation microstructures in garnet, titanite

816  and clinozoisite from an eclogite of the Lower Schist Cover, Tauern Window,

817  Austria. European Journal of Mineralogy 16(6):939-944 doi:10.1127/0935-

818  1221/2004/0016-0939

819   Nemchin A, Timms N, Pidgeon R, Geisler T, Reddy S, Meyer C (2009) Timing of

820   crystallization of the lunar magma ocean constrained by the oldest zircon. Nature

821   Geoscience 2(2):133-136 doi:10.1038/NGEO417

822   O'Neill C, Marchi S, Zhang S, Bottke W (2017) Impact-driven subduction on the

823   Hadean Earth. Nature Geoscience 10(10):793-797 doi:10.1038/ngeo3029

824   Papapavlou K, Darling JR, Storey CD, Lightfoot PC, Moser DE, Lasalle S (2017)

825   Dating shear zones with plastically deformed titanite: New insights into the orogenic

826   evolution of the Sudbury impact structure (Ontario, Canada). Precambrian Research

827   291:220-235 doi:10.1016/j.precamres.2017.01.007

828   Papapavlou K, Darling JR, Moser DE, Barker IR, White LF, Lightfoot PC, Storey

829   CD, Dunlop J (2018) U–Pb isotopic dating of titanite microstructures: potential

830   implications for the chronology and identification of large impact structures.

831   Contributions to Mineralogy and Petrology 173(10) doi:10.1007/s00410-018-1511-0

832   Prior DJ, Boyle AP, Brenker F, Cheadle MC, Day A, Lopez G, Peruzzo L, Potts GJ,

833   Reddy S, Spiess R, Timms NE, Trimby P, Wheeler J, Zetterström L (1999) The

834   application of electron backscatter diffraction and orientation contrast imaging in the

835   SEM to textural problems in rocks. American Mineralogist 84:1741-1759

836   Rae ASP, Morgan JVC, G. S. Grieve, R. A. F. Osinski, G. R. Salge, T., Hall B,

837   Ferrière L, Poelchau M, Gulick SPS, Scientists E (2017) Deformation, Shock

838   Barometry, and Porosity Within Shocked Target Rocks of the Chicxulub Peak Ring:

839   Results from IODP-ICDP Expedition 364. In: 48th Lunar and Planetary Science

840   Conference, vol., The Woodlands, Texas, p 1934

841   Rae ASP (2018) The Kinematics and Dynamics of Complex Crater Collapse. Imperial

842   College London

843  Reddy SM, Timms NE, Pantleon W, Trimby P (2007) Quantitative characterization of

844  plastic deformation of zircon and geological implications. Contributions to

845  Mineralogy and Petrology 153(6):625-645 doi:10.1007/s00410-006-0174-4

846  Reddy SM, Johnson TE, Fischer S, Rickard WDA, Taylor RJM (2015) Precambrian

847  reidite discovered in shocked zircon from the Stac Fada impactite, Scotland. Geology

848  43(10):899-902 doi:10.1130/g37066.1

849  Renne PR, Deino ALH, F.J., Kuiper KF, Mark DF, Mitchell WS, Morgan LE, Mundil

850  R, Smit J (2013) Time scales of critical events around the Cretaceous-Paleogene

851  boundary. Science 339(6120):684-687

852  Riller U, Poelchau MH, Rae ASP, Schulte FM, Collins GS, Melosh HJ, Grieve RAF,

853  Morgan JV, Gulick SPS, Lofi J, Diaw A, McCall N, Kring DA, Party I-IES (2018)

854  Rock fluidization during peak-ring formation of large impact structures. Nature

855  562(7728):511-518 doi:10.1038/s41586-018-0607-z

856  Salje E, Schmidt C, Bismayer U (1993) Structural phase transition in titanite,

857  $CaTiSiO_5$: A Ramanspectroscopic study. Physics and Chemistry of Minerals

858  19(7):502-506

859  Schmieder M, Kring DA, Lapen TJ, Gulick SPS, Stockli DF, Rasmussen C, Rae ASP,

860  Ferrière L, Poelchau M, Xiao L, Wittmann A (2017) Sphene and $TiO_2$ assemblages in

861  the Chicxulub peak ring: U-Pb systematics and implications for shock pressures,

862  temperatures, and crater cooling. Meteoritics & Planetary Science 52:A308-A308

863  Schulte P, Alegret L, Arenillas I, Arz JA, Barton PJ, Bown PR, Bralower TJ,

864  Christeson GL, Claeys P, Cockell CS, Collins GS (2010) The Chicxulub asteroid

865  impact and mass extinction at the Cretaceous-Paleogene boundary. Science

866  327(5970):1214-1218

867    Speer JA, Gibbs GV (1976) The crystal structure of synthetic titanite, $CaTiOSiO_4$,

868    and the domain textures of natural titanites. American Mineralogist 61(3-4):238-247

869    Taylor M, Brown GE (1976) High-temperature structural study of the $P2_1/a$<--> A2/a

870    phase transition in synthetic titanite, $CaTiSiO_5$. American Mineralogist 61(5-6):435-

871    447

872    Thomson OA, Cavosie AJ, Moser DE, Barker I, Radovan HA, French BM (2014)

873    Preservation of detrital shocked minerals derived from the 1.85 Ga Sudbury impact

874    structure in modern alluvium and Holocene glacial deposits. Geological Society of

875    America Bulletin 126(5-6):720-737 doi:10.1130/b30958.1

876    Timms NE, Reddy SM, Healy D, Nemchin AA, Grange ML, Pidgeon RT, Hart R

877    (2012) Resolution of impact-related microstructures in lunar zircon: A shock-

878    deformation mechanism map. Meteoritics & Planetary Science 47(1):120-141

879    doi:10.1111/j.1945-5100.2011.01316.x

880    Timms NE, Erickson TM, Zanetti M, Pearce MA, Cayron C, Cavosie AJ, Reddy SM,

881    Wittmann A, Carpenter PK (2017a) Cubic zirconia in >2370 °C impact melt records

882    Earth's hottest crust. Earth and Planetary Science Letters 477(1):52-58

883    doi:https://doi.org/10.1016/j.epsl.2017.08.012

884    Timms NE, Erickson TM, Pearce MA, Cavosie AJ, Schmieder M, Tohver E, Reddy

885    SM, Zanetti M, Nemchin AA, Wittmann A (2017b) A pressure-temperature phase

886    diagram for zircon at extreme conditions. Earth Science Reviews 165:185-202

887    doi:10.1016/j.earscirev.2016.12.008

888    Timms NE, Healy D, Erickson TM, Nemchin AA, Pearce MA, Cavosie AJ (2018)

889    Role of elastic anisotropy in the development of deformation microstructures in

890    zircon. In: Moser D, Corfu F, Reddy S, Darling J, Tait K (eds) Microstructural

891    Geochronology: Planetary Records Down to Atom Scale, Geophysical Monograph

892    232, vol. AGU-Wiley, pp 183-202

893    Wheeler J, Prior D, Jiang Z, Spiess R, Trimby P (2001) The petrological significance

894    of misorientations between grains. Contributions to Mineralogy and Petrology

895    141(1):109-124 doi:10.1007/s004100000225

896    Wheeler J, Mariani E, Piazolo S, Prior DJ, Trimby P, Drury MR (2009) The weighted

897    Burgers vector: a new quantity for constraining dislocation densities and types using

898    electron backscatter diffraction on 2D sections through crystalline materials. Journal

899    of Microscopy 233(3):482-494

900    White LF, Darling JR, Moser DE, Cayron C, Barker I, Dunlop J, Tait KT (2018)

901    Baddeleyite as a widespread and sensitive indicator of meteorite bombardment in

902    planetary crusts. Geology 46(8):719-722 doi:10.1130/g45008.1

903    Whitney DL, Evans BW (2009) Abbreviations for names of rock-forming minerals.

904    American Mineralogist 95(1):185-187 doi:10.2138/am.2010.3371

905    Wittmann A, Kenkmann T, Schmitt RT, Stöffler D (2006) Shock-metamorphosed

906    zircon in terrestrial impact craters. Meteoritics & Planetary Science 41(3):433-454

907    Zhao JW, Xiao L, Liu HS, Xiao ZY, Morgan J, Gulick S, Kring D, Claeys P, Riller U,

908    Wittmann A, Ferriere L (2017) Shock Metamorphic Effects of the Peak Ring Granites

909    within the Chicxulub Crater. Lunar and Planetary Science Conference Proceedings
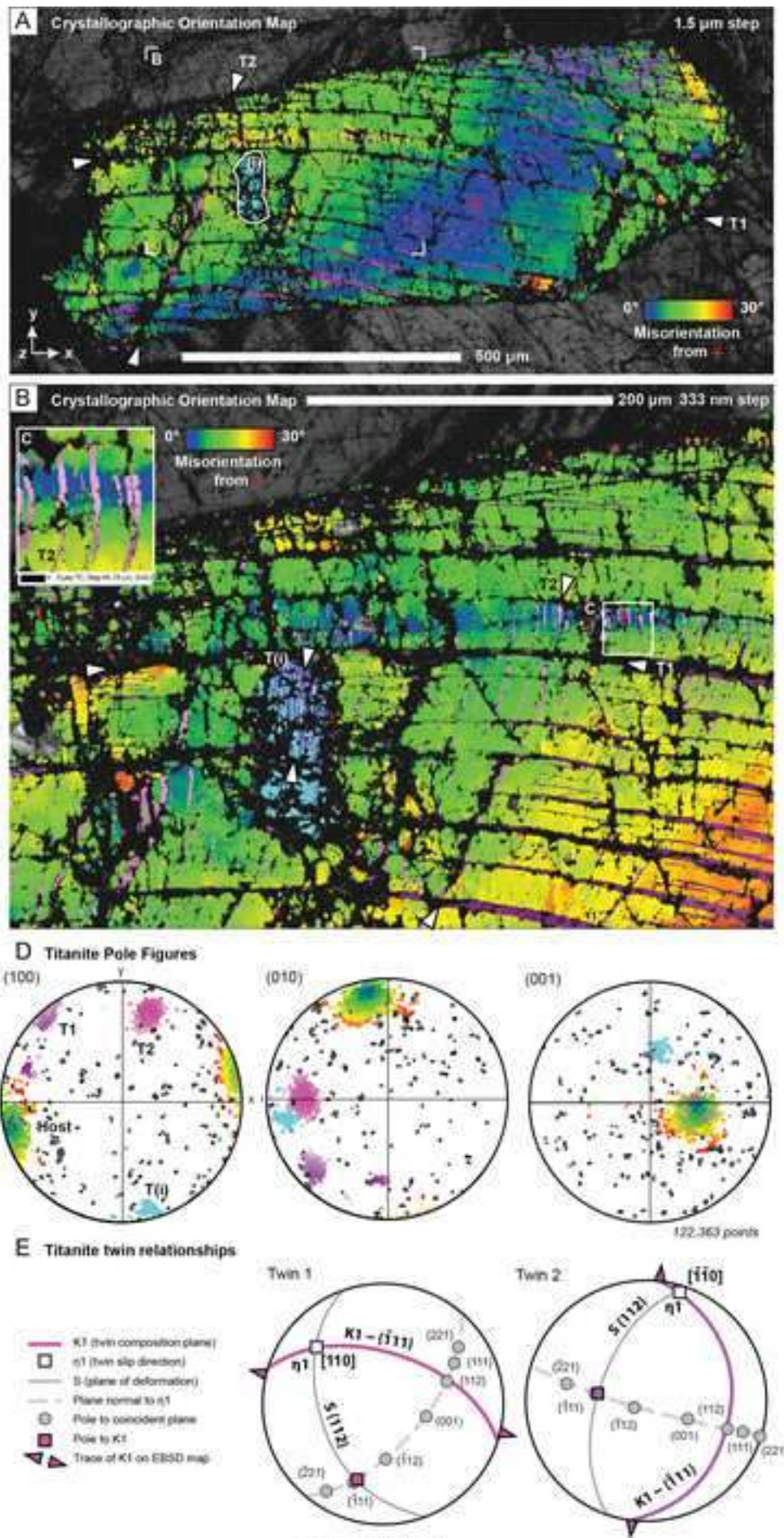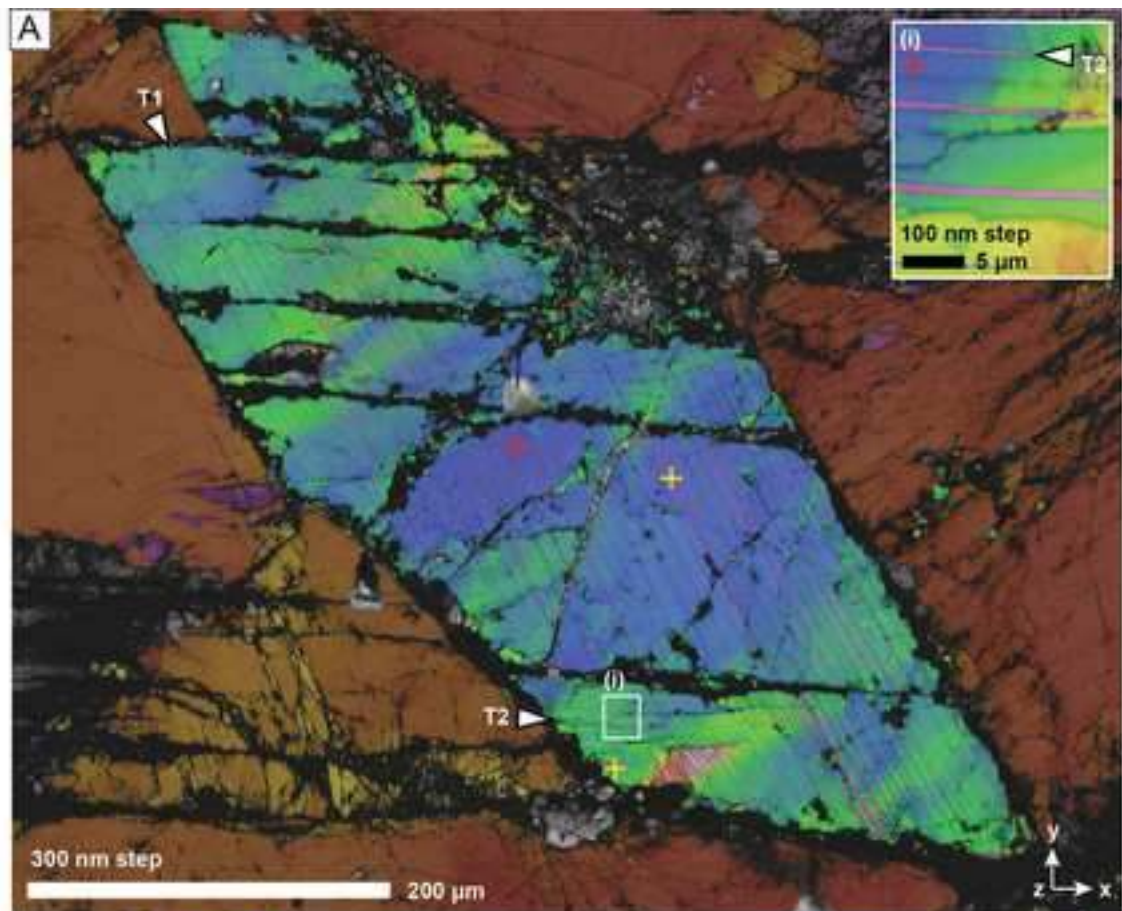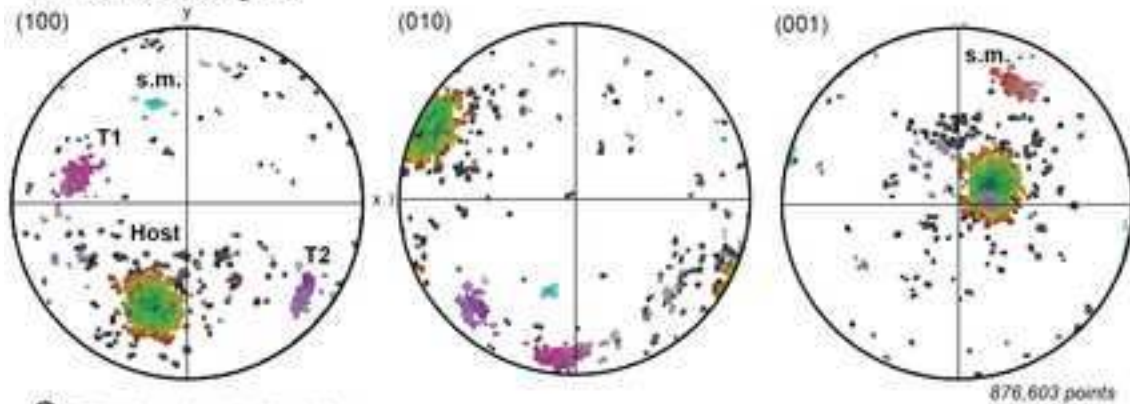
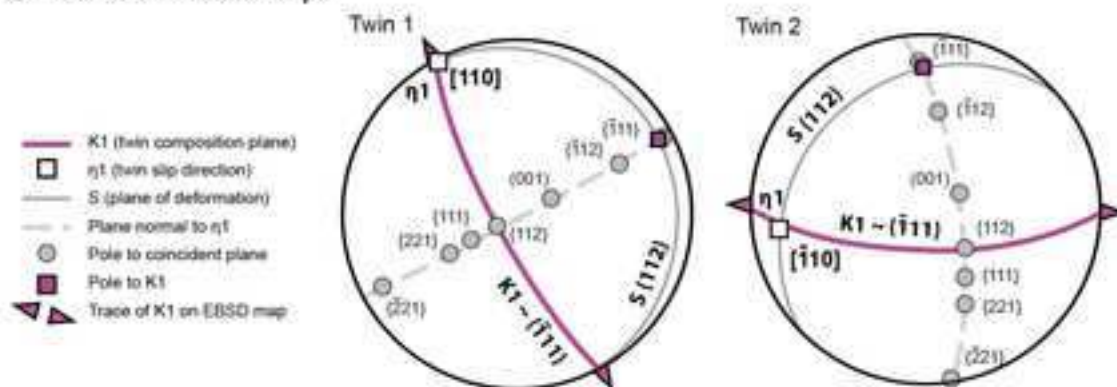910    48:1421

911
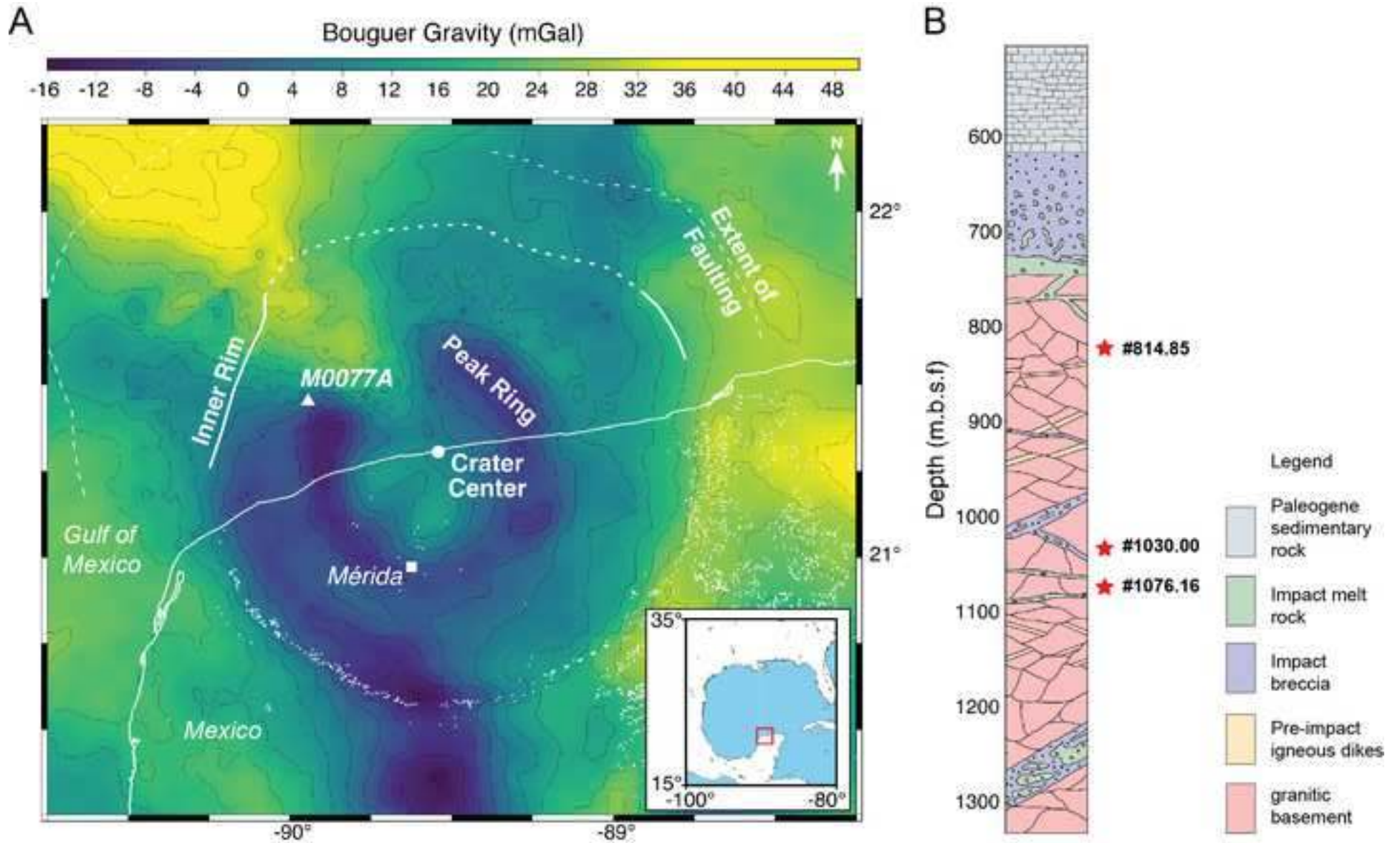
*Timms Figure 1*
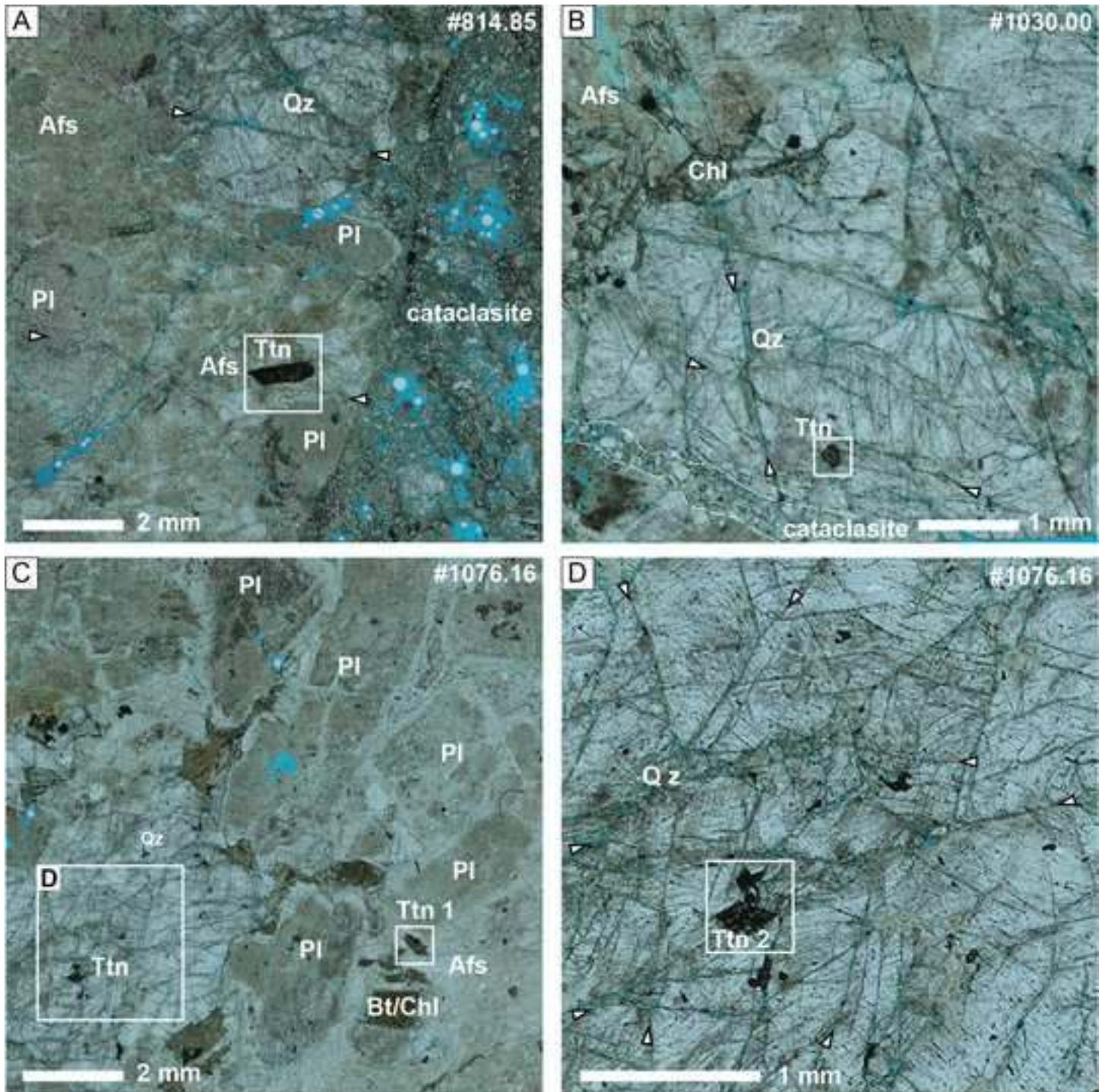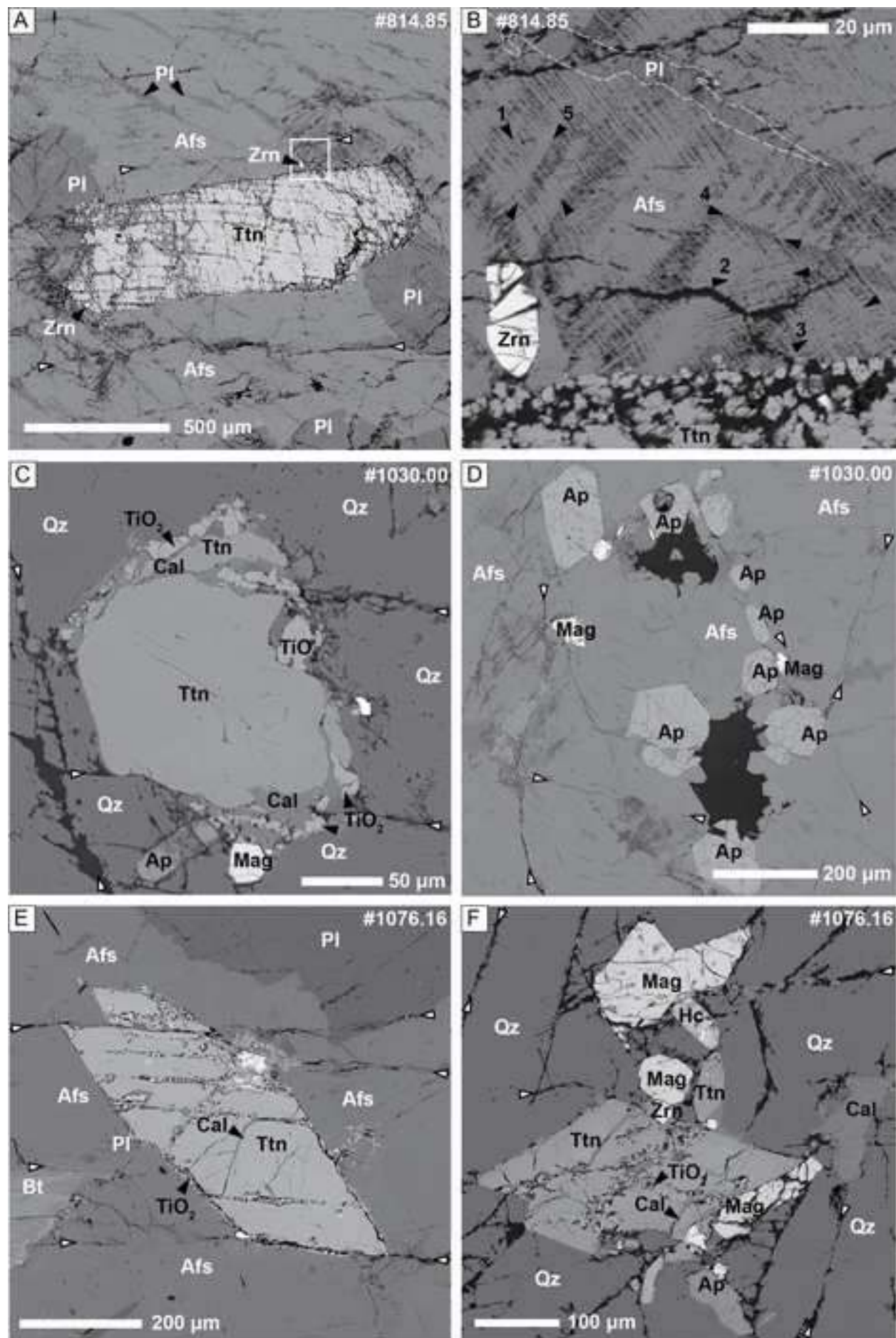
Figure 2

Timms Figure 2

*Timms Figure 3*
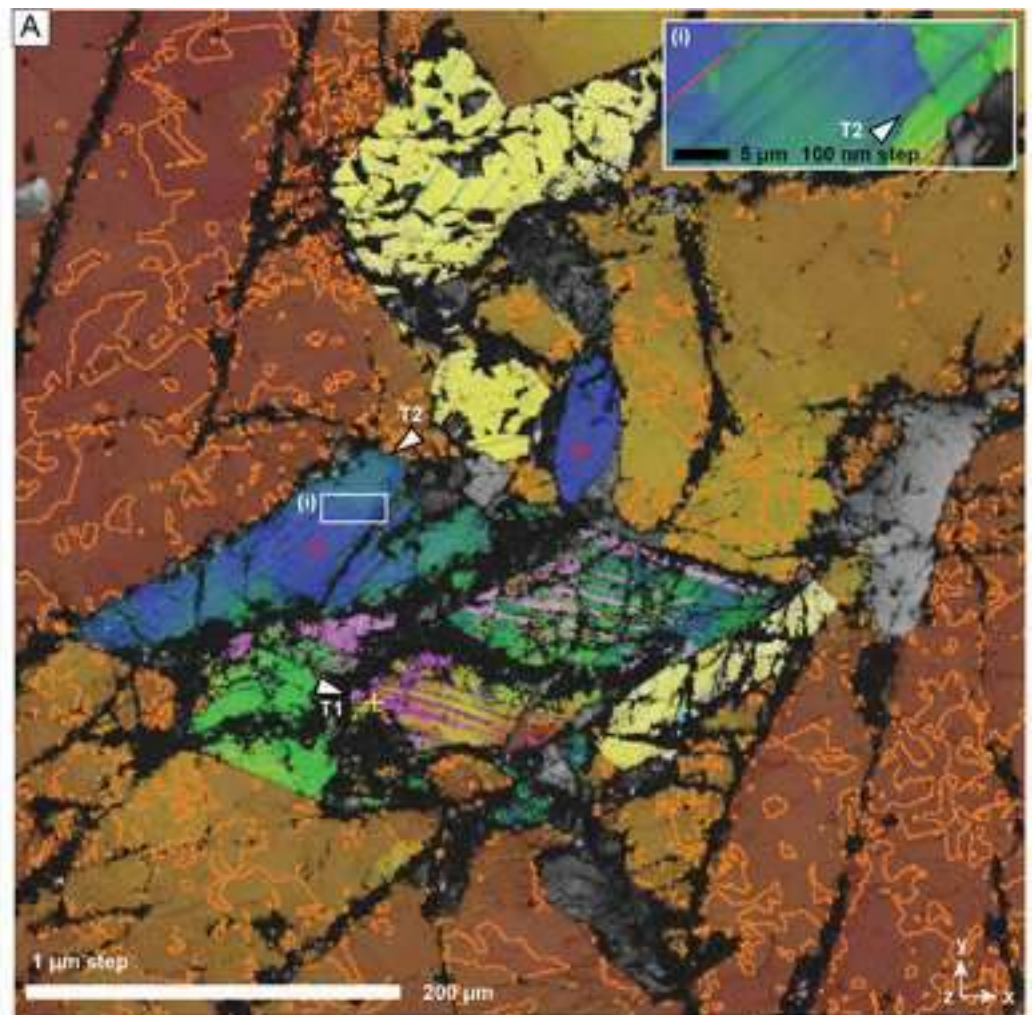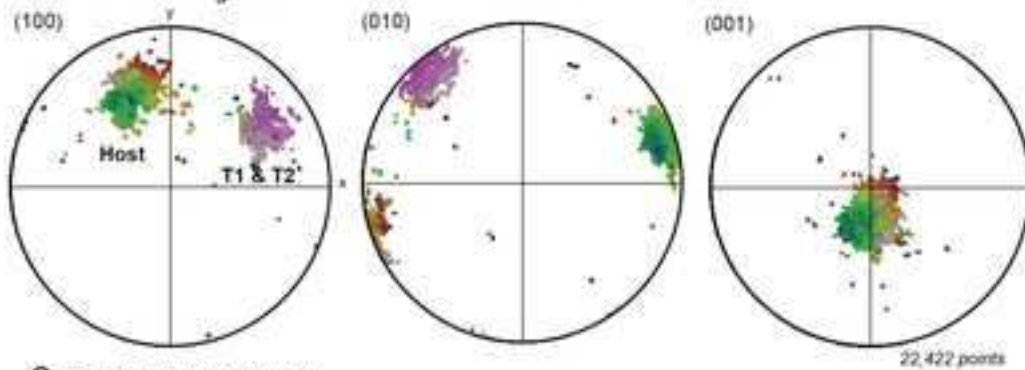
Figure 4

*Timms Figure 4*
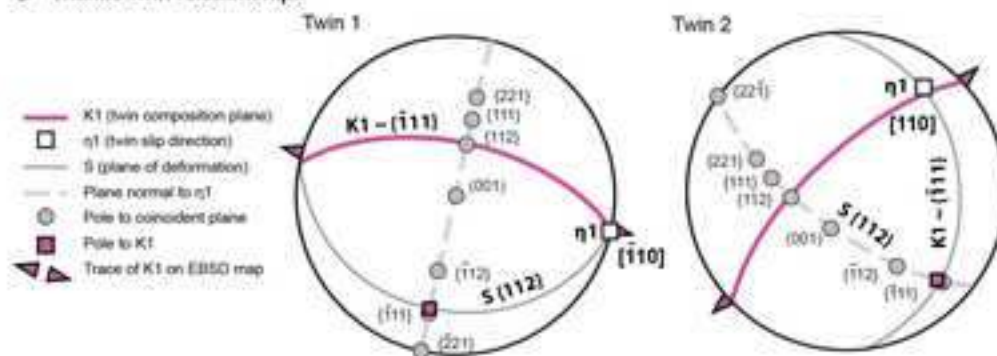
Figure 5

*Timms Figure 5*

Figure 6

*Timms Figure 6*
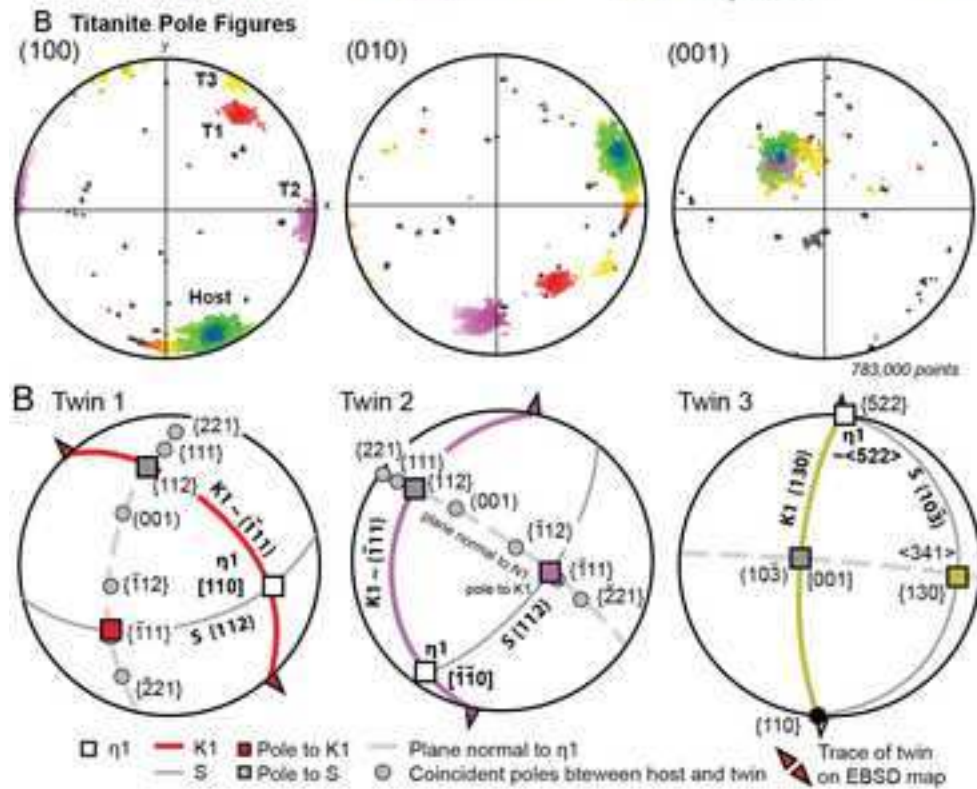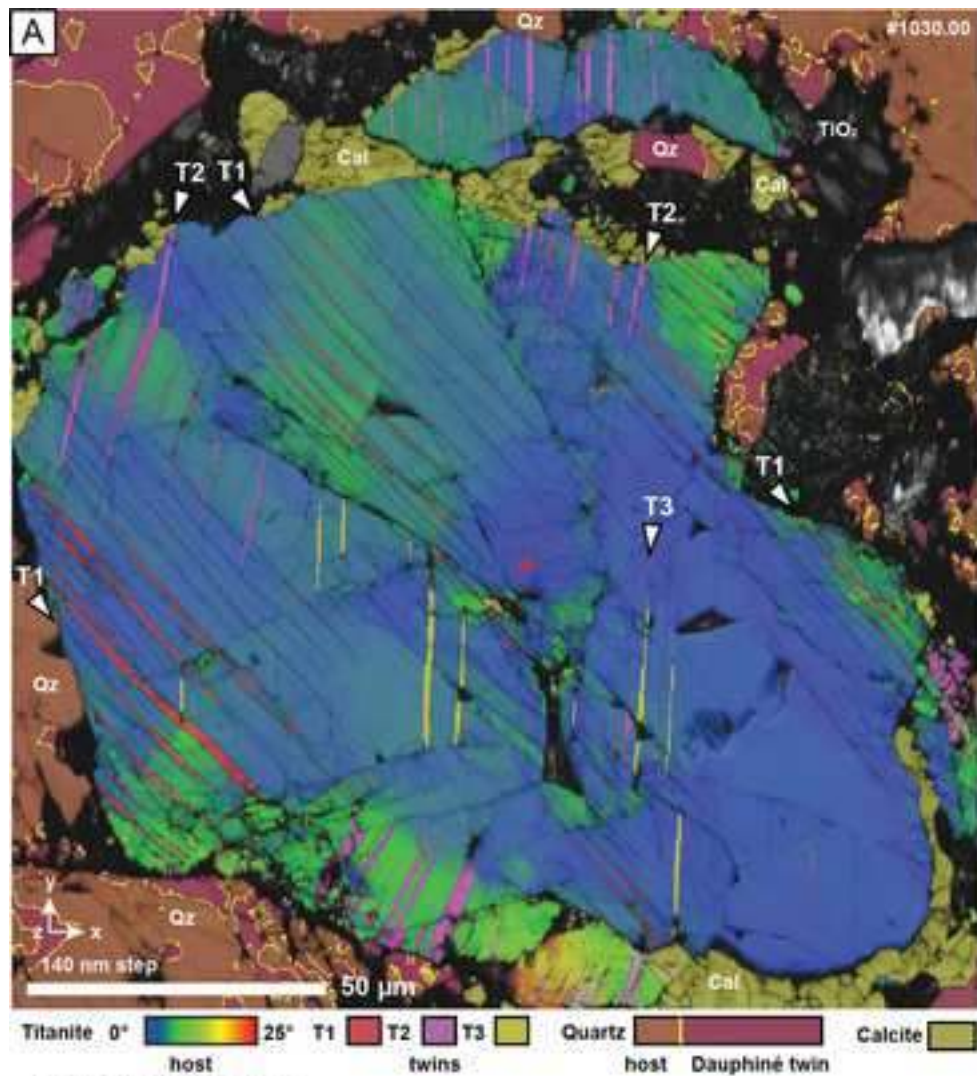
Figure 7

*Timms Figure 7*

*Timms Figure 8*
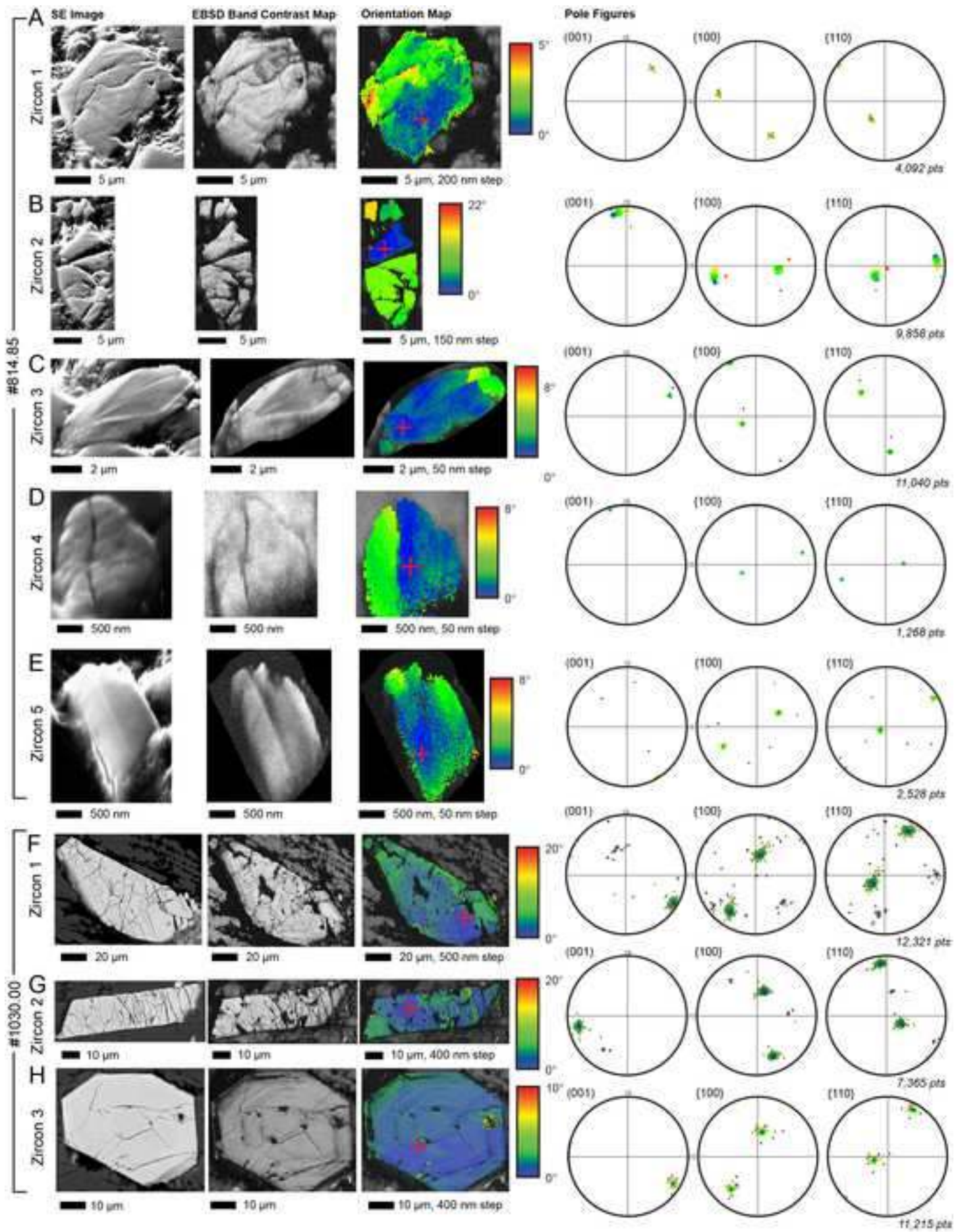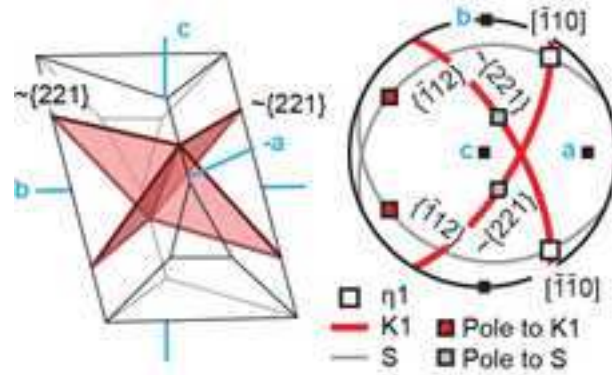
Figure 9

*Timms Figure 9*

Figure 10

Timms Figure 10

Timms et al. Figure 11
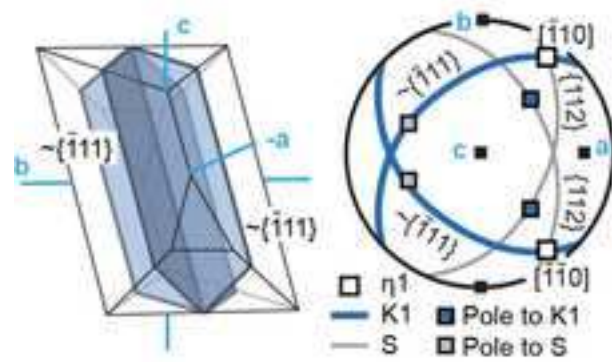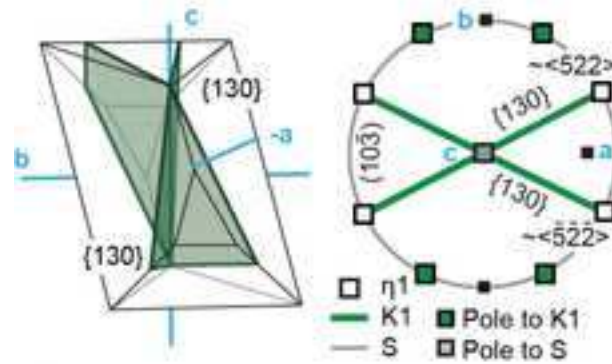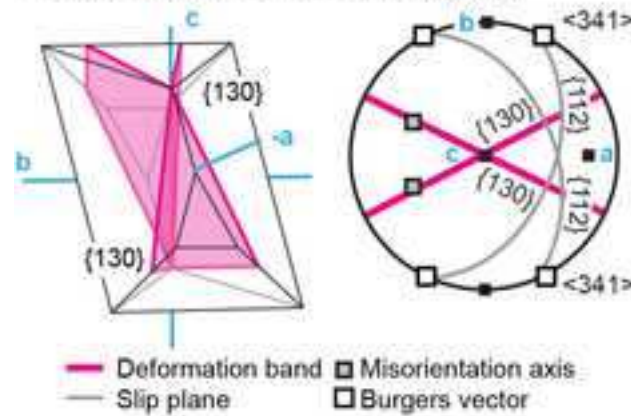
Table 1

**Table 1**. Details of samples used in this study. Sample IDs comprise information relating to the IODP catalogue system, and have the following naming convention: Expedition-Site-Hole-Core-Section-TopDepth-BottomDepth. Depths are driller depths given as metres below sea floor (m.b.s.f).

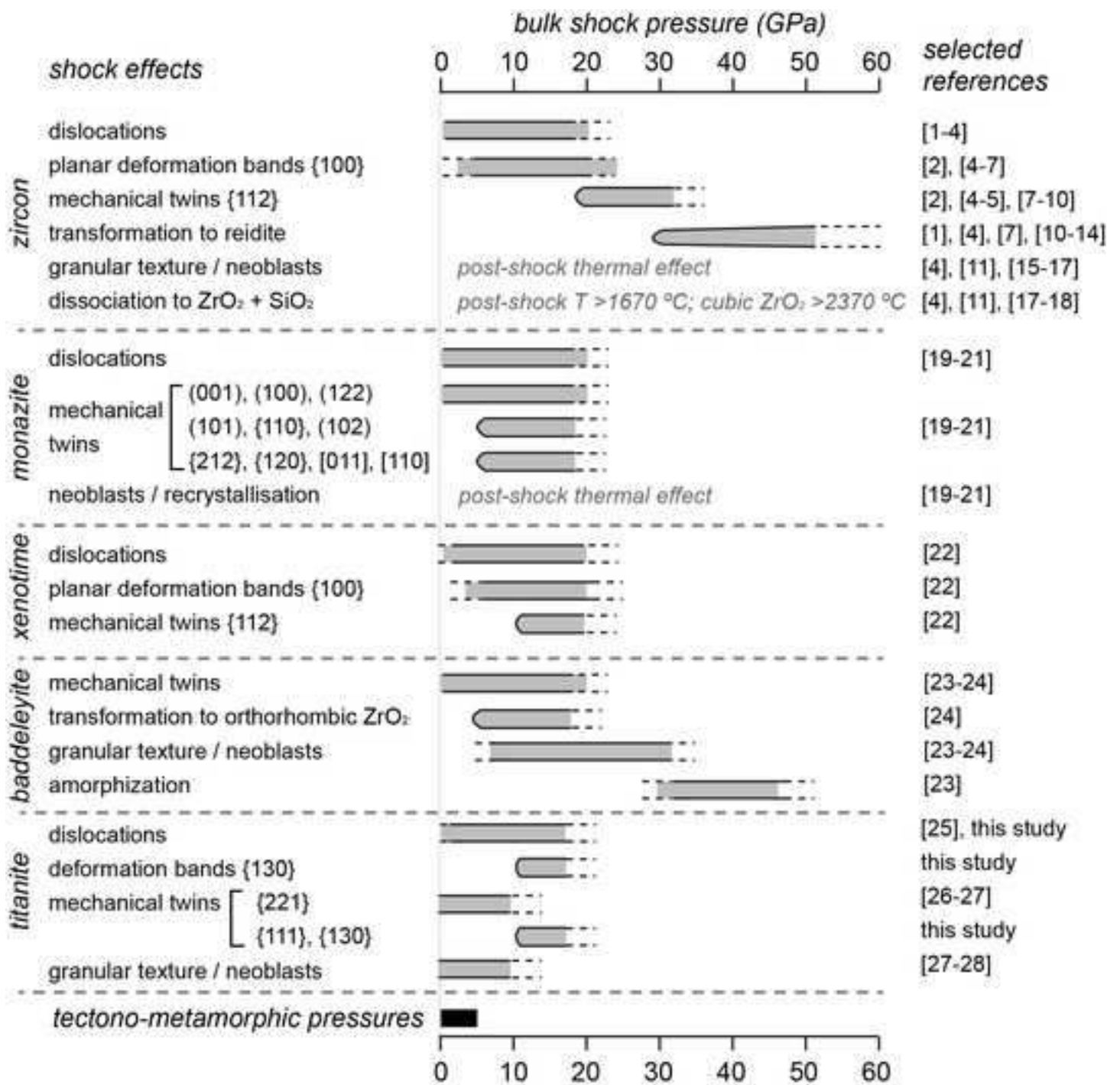| IODP Sample ID | Depth (m.b.s.f.) | Brief thin section description |
|---|---|---|
| 364-77-A-121-R-1-75-77 | 814.85 | Shocked granitoid with thick cataclasite bands. Intact domains are dominated by plagioclase and alkali feldspar with perthite lamellae and local PDFs. Subordinate patches of quartz have abundant PFs and PDFs. Minor chlorite after biotite, and euhedral titanite. Accessory apatite, zircon and magnetite. Cataclasite contains patchy calcite cement. |
| 364-77-A-204-R-1-7-9 (duplicate) | 1030.00 | Shocked granitoid dominated by large plagioclase laths and alkali feldspar with perthite lamellae, subordinate quartz patches with abundant PFs and PDFs. Minor biotite (partially altered to chlorite) and euhedral titanite. Accessory apatite, magnetite, and zircon. Conspicuous set of transgranular planar fractures are lined with calcite. |
| 364-77-A-219-R-1-22-24 | 1076.16 | Shocked granitoid with roughly equal proportions of plagioclase, alkali feldspar and quartz. Quartz contains abundant PFs and PDFs. Minor biotite (heterogeneously altered to chlorite), euhedral titanite and apatite. Accessory magnetite, zircon, and hercynite. Alkali feldspar contains perthite lamellae. Patchy calcite lines fractures. |

Table 2

**Table 2**. Scanning electron microscopy settings and electron backscatter diffraction analysis acquisition and processing parameters.

| SEM | | | | |
|---|---|---|---|---|
| Make/model | | Tescan Mira3 FEG-SEM | | |
| EBSD acquisition system | | Oxford Instruments AZtec / Nordlys EBSD Detector | | |
| EDX acquisition system | | Oxford Instruments AZtec / XMax 20 mm SDD | | |
| EBSD Processing software | | Oxford Instruments Channel 5.10 | | |
| Acceleration Voltage (kV) | | 20 | | |
| Working Distance (mm) | | 18.5 | | |
| Tilt | | 70° | | |
| **EBSD match units** | | | | |
| *Phase* | *Space Group* | *β (°)* | | |
| Titanite | 15 | 113.93 | American Mineralogist phase database (database family 725, best in family) | |
| Quartz | 152 | n/a | 'Quartznew', HKL database (Sands, 1969) | |
| Orthoclase | 12 | 116.07 | American Mineralogist phase database (Prince et al., 1973) | |
| Bytownite | 2 | 115.87 | ICSD phase database (Facchinelli et al., 1979) | |
| Magnetite | 227 | n/a | HKL phase database (Wechsler et al., 1984) | |
| Calcite | 0 | n/a | HKL phase database (calcite.cry) | |
| Zircon | 141 | n/a | Zircon5260, 1 atm (Hazen and Finger, 1979) | |
| Reidite | 88 | n/a | Reidite6032 0.69 GPa (Farnan et al., 2003) | |
| Apatite | 176 | n/a | ICSD phase database (Gankev, 1996) | |
| **EBSP Acquisition, Indexing and Processing** | | | | |
| EBSP Acquisition Speed (Hz) | 40 | Band detection (min / max) | | 6 / 8 |
| EBSP Background (frames) | 64 | Mean mean angular deviation (all phases) | | <1° |
| EBSP Binning | 4 x 4 | Wildspike correction | | Yes |
| EBSP Gain | High | Nearest neighbor zero solution extrapolation | | 8 |
| Hough resolution | 60 | | | |

Table 3

**Table 3**. Unit cell parameters for titanite

| A (Å) | 6.554 |
|-------|-------|
| B (Å) | 8.708 |
| C (Å) | 7.069 |
| α (°) | 90 |
| β (°) | 113.93 |
| γ (°) | 90 |

Table 4

**Table 4**. Host-twin disorientation and misorientation calculations for titanite

| Grain and twin ID | Disorientation | | 180° Misorientation | | | | |
|---|---|---|---|---|---|---|---|
| | | | *Angle (°)* | ***Best fit plane normal*** | | ***Best-fit direction*** | |
| | *Angle (°)* | *Axis <hkl>* | | *Plane {hkl}* | *Deviation (°)* | *Axis {hkl}* | *Deviation (°)* |
| 121 T1 | 75.23 | 102 | 179.92 | $\bar{1}\bar{1}0$ | 0.66 | $24\bar{1}$ | 4.53 |
| 121 T2 | 72.27 | $\bar{1}0\bar{2}$ | 179.33 | $1\bar{1}0$ | 1.59 | $2\bar{4}\bar{1}$ | 2.60 |
| 121 T(i) | 73.32 | 102 | 179.34 | $\bar{1}\bar{1}0$ | 0.67 | $24\bar{1}$ | 4.01 |
| 204 T1 | 74.16 | 102 | 179.98 | 110 | 0.23 | $24\bar{1}$ | 4.12 |
| 204 T2 | 74.02 | 102 | 179.65 | $\bar{1}\bar{1}0$ | 0.22 | $24\bar{1}$ | 4.07 |
| 204 T3 | 51.30 | 001 | 179.97 | $\bar{3}\bar{4}\bar{1}$ | 2.11 | $\bar{1}\bar{3}0$ | 0.20 |
| 219_1 T1 | 73.93 | $\bar{1}0\bar{2}$ | 179.93 | $\bar{1}10$ | 0.08 | $2\bar{4}\bar{1}$ | 3.88 |
| 219_1 T2 | 74.17 | $\bar{1}0\bar{2}$ | 176.85 | $\bar{1}10$ | 0.73 | $2\bar{4}\bar{1}$ | 4.37 |
| 219_2 T1 | 72.12 | 102 | 178.20 | 110 | 1.06 | $24\bar{1}$ | 3.53 |
| 219_2 T2 | 72.58 | 102 | 179.98 | $\bar{1}\bar{1}0$ | 0.75 | $24\bar{1}$ | 3.18 |
| Borg 1970 | ~73 | 102 | 180 | 110 | n/a | 221 | n/a |

Table 5

**Table 5**. Twinning in titanite. Disorientation = angle/axis that describes the minimum misorientation between the twin and the host. 'Coincidence' is defined as <0.7° angular deviation.

| Source Reference | Borg (1970) | Borg (1970) | This study | This study |
|---|---|---|---|---|
| Examples | | | #814.85 (T1, T2), #1030.00 (T1, T2), #1076.16_1 (T1, T2), #1076.16_2 (T1, T2) | #1030.00 (T3) |
| **Twin Mode** | | | | |
| $K_1$ (slip plane, plane of no distortion, composition plane) | Irrational ~{221} | {$\bar{1}$31} | Irrational ~{$\bar{1}$11} | {130} |
| $\eta_1$ (Slip direction) | <110> | Irrational | <110> | Irrational ~<522> |
| $K_2$ (Conjugate plane of no distortion) | {$\bar{1}$31} | Irrational ~{221} | Rational ??? | ??? |
| $\eta_2$ (axis of principal zone) | Irrational | <110> | ??? | ??? |
| S (plane of deformation) | Irrational ~{$\bar{1}\bar{1}$2} | | {112} | (10$\bar{3}$) |
| Twin type | 2 | 1 | 2 | 1 |
| **Disorientation** | | | | |
| Angle | ~74° | ~74° | ~74° | ~53° |
| Axis | <102> | <102> | <102> | [003] |
| **Coincident Planes** | | | | |
| (001) | | | Yes | No |
| {111} | | | Yes | No |
| {$\bar{1}$11} | | | Yes | No |
| {112} | | | Yes | No |
| {$\bar{1}$12} | | | Yes | No |
| {221} | | | Yes | No |
| {22$\bar{1}$} | | | Yes | No |
| {24$\bar{1}$} | | | (Yes?) | No |
| {130} | | | No | Yes |
| ($\bar{1}$03) | | | No | Yes |
| | | | | |
| **Coincident directions** | | | | |
| [001] | | | No | Yes |
| <110> | | | Yes | No |
| <$\bar{1}$10> | | | Yes | No |
| <$\bar{3}\bar{4}\bar{1}$> | | | No | No |